# A global dust emission dataset for estimating dust radiative forcings in climate models

Danny M. Leung[1,2], Jasper F. Kok[1], Longlei Li[3], David M. Lawrence[4], Natalie M. Mahowald[3], Simone
5  Tilmes[2], and Erik Kluzek[4]

[1]Department of Atmospheric and Oceanic Sciences, University of California – Los Angeles, Los
Angeles, California, USA
[2]Atmospheric Chemistry Observations and Modeling Laboratory, NSF National Center for Atmospheric
10  Research, Boulder, Colorado, USA
[3]Department of Earth and Atmospheric Sciences, Cornell University, Ithaca, New York, USA
[4]Climate and Global Dynamics Laboratory, NSF National Center for Atmospheric Research, Boulder,
Colorado, USA

15  *Correspondence to*: Danny M. Leung (dleung@ucar.edu)

## Abstract

20       Sedimentary records indicate that atmospheric dust has increased substantially since preindustrial
times. However, state-of-the-art global Earth system models (ESMs) are unable to capture this historical
increase, posing challenges in assessing the impacts of desert dust on Earth's climate. To address this
issue, we construct a globally gridded dust emission dataset (DustCOMMv1) spanning 1841–2000. We
do so by combining 19 sedimentary records of dust deposition with observational and modeling
25  constraints on the modern-day dust cycle. The derived emission dataset contains interdecadal variability
of dust emissions as forced by the deposition flux records, which increased by approximately 50% from
the 1850s to the 1990s. We further provide future dust emission datasets for 2000–2100 by assuming three
possible scenarios for how future dust emissions will evolve. We evaluate the dust emission dataset and
illustrate its effectiveness in enforcing a historical dust increase in ESMs by implementing conducting a
30  long-term (1851–2000) dust cycle simulation with the Community Earth System Model (CESM2). The
simulated dust deposition is in reasonable agreement with the long-term increase in most sedimentary dust
deposition records and with measured long-term trends in dust concentration at sites in Miami and
Barbados. This contrasts with the CESM2 simulations using a process-based dust emission scheme and
with simulations from the Coupled Model Intercomparison Project (CMIP6), which show little to no
35  secular trends in dust deposition, concentration, and optical depth. The DustCOMM emissions thus
enables ESMs to account for the historical radiative forcings (RFs), including due to dust direct
interactions with radiation (direct RF). Our CESM2 simulations estimate a 1981–2000 minus 1851–1870
direct RF of –0.10 W m$^{-2}$ from dust particles up to 10 μm in diameter (PM$_{10}$).

40

## 1 Introduction

45

Observations indicate that desert dust in the atmosphere has increased by about 50 % since the 1850s (e.g., Mahowald et al., 2010; Hooper and Marx, 2018; Kok et al., 2023). It is crucial that Earth system models (ESMs) and chemical transport models (CTMs) simulate this dust increase to adequately represent its impacts on climate, ocean nutrient cycles, and ecosystems. However, state-of-the-art ESMs
50 struggle to capture this historical increase in desert dust (Kok et al., 2023). While global models can reasonably represent the global spatial distribution of dust in the contemporary climate (e.g., Zhao et al., 2022), they struggle to represent the temporal variability of dust (e.g., Klose et al., 2021; Kok et al., 2023). Many ESM dust simulations can roughly capture the day-to-day variability and seasonality of dust (e.g., Klose et al., 2021; Leung et al., 2024), but they fail to capture the historical interannual to interdecadal
55 variability (e.g., Mahowald et al., 2010; Smith et al., 2017; Evan, 2018; Kok et al., 2023). Most historical of the Coupled Model Intercomparison Project phase 6 (CMIP6) ESMs showed flat dust trends across 1850–2000, while sedimentary records showed a dust increase of 55±30 % for the same period (Kok et al., 2023).

60 The large observed historical dust increase is thought to be mainly due to historical human land-use and land-cover change (LULCC) and climate change (Stanelle et al., 2014). For example, the global agricultural area increased from ~9 % in the 1850s to ~35 % in the 2000s (Klein Goldewijk et al., 2011). The large-scale conversion of wildlands to agricultural land across many semiarid regions could have resulted in significant desertification and elevated dust emissions across the globe (McConnell et al., 2007;
65 Neff et al., 2008; Ginoux et al., 2012; Webb and Pierre, 2018). Human water use management as well as climate change could also result in the desiccation of inland lakes and the formation of playas, which then emit salted dust (e.g., Niemeyer et al., 1999; Indoitu et al., 2015; Xi and Sokolik, 2016). Furthermore, global biological soil crust (biocrust) cover on land surfaces have been shown to reduce under human-induced land-use and climate changes (e.g., trampling by livestocks and vehicles, perturbed temperature
70 and precipitation), further enhancing dust emissions (Ferrenberg et al., 2015; Rodriguez-Caballero et al., 2018, 2022). In addition, climate change could enhance dust emissions via multiple pathways, such as enhanced aridity over arid regions (Held and Soden, 2006; Pu and Ginoux, 2017), increased soil bareness due to increased wildfires (Wagner et al., 2021; Yu and Ginoux, 2022; Wang et al., 2023), and elevated wind speed over some desert regions (Masson-Delmotte et al., 2021; Yu and Ginoux, 2022). Climate
75 change might also reduce dust emissions, such as by enhancing vegetation cover and reducing bareness via $CO_2$ fertilization (e.g., Smith et al., 2000; Mahowald, 2007). Although many ESMs include the processes necessary to represent climate change and LULCC, they are unable to reproduce the secular dust trend. This model–observation discrepancy is likely in part because ESM dust emission schemes are not sufficiently sensitive to the input variables of wind speed, soil moisture, and soil bareness in ESMs
80 (e.g., Kok et al., 2014, 2018). It could also possibly be because the climate change and LULCC over the arid regions in ESMs are not well represented, such as by missing biocrust degradation or other processes. Investigating the main drivers of this dust trend, and improving the ESM representation of it, are thus necessary for accounting for the impacts of the historical and future dust changes on the Earth system.

85 The major problem of the ESMs' missing long-term dust trend is that ESMs will not capture the radiative forcing (RF) due to the increased dust and its interactions with radiation, clouds, atmospheric chemistry, snow and ice, and biogeochemistry (Kok et al., 2023). Furthermore, since current estimates of the climate sensitivity (K or K $W^{-1}$ $m^2$) to greenhouse gas (GHG) warming depend on the historical aerosol RF, missing the dust RF likely causes ESMs to underestimate the overall negative aerosol RF, which could
90 in turn affect models' climate sensitivity (e.g., Andreae et al., 2005; Mahowald et al., 2024). Hence, the inadequate representation of the historical dust increase in ESMs may affect RFs, climate sensitivity, and

ultimately mislead climate change predictions, such as those reported by the Intergovernmental Panel on Climate Change (IPCC, 2021).

95   Despite the inability of models to represent the historical increase in desert dust, previous studies have estimated the effects of this increase on Earth's radiation budget and climate (Mahowald et al., 2010; Stanelle et al., 2014; Kok et al., 2023):

$$RF_{historical} \equiv RE_{2000s} - RE_{1850s} \approx RE_{2000s} \times f_{\Delta dust}, \tag{1}$$

where $f_{\Delta dust}$ represents the fractional change in dust mass loading for 1850–2000. Here, the radiative
100   effect (RE; W m$^{-2}$) of dust is defined as the change in the Earth's radiation budget due to the presence of dust at a given time (e.g., in year 1850), and the RF is defined as the change in RE across time (e.g., from 1850 to 2000), which could be due to changes in dust mass and/or other dust properties. The uncertainty in dust RF is thus partially due to uncertainty in the quantification of dust RE, which itself is a sum of REs due to dust interactions with radiation, cloud microphysics, atmospheric chemistry, biogeochemistry, and
105   the cryosphere (Mahowald et al., 2010; Storelvmo, 2017; Skiles et al., 2018; Hamilton et al., 2022). Of these various dust radiative effects, the direct radiative effect (DRE) of dust, due to dust scattering and absorbing radiation, is the best understood, while dust indirect REs are less understood due to the highly complex and uncertain modeled dust interactions with other processes (e.g., Boucher et al., 2013; Storelvmo, 2017; Bellouin et al., 2020). The DRE depends on multiple factors, such as the dust particle
110   size distribution (PSD), dust mineralogy, as well as the albedo of the underlying land surface (Li and Sokolik, 2018; Ke et al., 2022; Kok et al., 2023). ESMs thus need to prescribe adequate dust microphysical properties and simulate a realistic global dust distribution to estimate the dust DRE. However, current ESMs commonly overestimate fine dust (volume equivalent diameter $D_{ve} < 2.5$ μm), which cools by scattering shortwave (SW) radiation, and neglect or underestimate super-coarse dust ($D_{ve} > 10$ μm), which
115   tend to warm by absorbing SW and longwave (LW) radiation (Kok et al., 2017; Di Biagio et al., 2020; Adebiyi et al., 2023). Moreover, models neglect the warming effects of dust scattering of LW radiation (Dufresne et al., 2002; Di Biagio et al., 2020) and are subject to large uncertainties due to poorly constrained dust optical properties (Li et al., 2021a), with a possible bias towards dust that is too absorbing (Adebiyi et al., 2023). Considering all these uncertainties, current best estimates of the dust DRE are
120   within the range of –0.15 ± 0.35 W m$^{-2}$, reflecting that the sign of the dust DRE is unclear (Kok et al., 2023 and references therein). The dust DRE could thus slightly warm or moderately cool the Earth, depending on prescribed optical properties and the ratio of fine to coarse dust in the ESMs.

In addition to the uncertainty in the dust DRE and other dust REs, the estimation of dust RF is also
125   affected by our limited understanding of the historical dust change ($f_{\Delta dust}$). Recent advances in the estimation of historical dust change is informed by sedimentary records of dust deposition (e.g., McConnell et al., 2007; Mulitza et al., 2010; Clifford et al., 2019). There are > 30 such records that resolve the preindustrial to modern time period (Mahowald et al., 2010; Hooper and Marx, 2018; Kok et al., 2023), but only ~20 of these are thought to be moderately representative of long-range transported dust from the
130   major low-latitude source regions (Hooper and Marx, 2018). Nonetheless, previous studies (e.g., Mahowald et al., 2010; Kok et al., 2023) have used these deposition records to reconstruct the evolution of the global dust cycle since preindustrial times. (Kok et al., 2021a, b, 2023) further showed that one could statistically derive historical dust emission changes from the observed dust depositions using ESM-simulated deposition–emission relationships. This could enable ESMs to read in derived dust emissions
135   that encapsulate the observed historical dust trend. Using prescribed emissions can thus force more realistic ESM simulations of the dust cycle and dust RF that match the $f_{\Delta dust}$ inferred from dust deposition records, which current ESMs cannot reproduce using mechanistic emission schemes.

In this study, we use the existing sedimentary dust records to derive a global dust emission dataset and evaluate its effectiveness in representing the historical dust changes as exhibited by the records. We first combine sedimentary records of dust deposition with modeling and observational constraints to derive a global gridded dust emission dataset for 1841–2000. The emission dataset represents decadal dust trends constrained by the interdecadal variability of 19 dust deposition time series, and a gridded spatial dust variability informed by a multimodel ensemble (MME) estimate of the global dust emission spatial distribution and the observationally constrained dust size and optical properties. We then evaluate the derived emission dataset by enabling an ESM (in this study the Community Earth System Model version 2, CESM2) to read in the decadally-varying emission dataset and perform a historical simulation for 1851–2000. We compare the simulated dust cycle against available long-term dust observations to evaluate the performance of the ESM using the emission forcing. We finally compute the dust direct REs and RFs across the historical period using the ESM forced by the emission dataset. We show that ESMs employing this emission inventory are able to simulate the decadal variability of multiple dust cycle variables, hence enabling ESMs to predict more realistic dust RF and climatic impacts.

The paper is organized as follows. Section 2 provides a detailed discussion on deriving a globally gridded dust emission dataset for historical and future conditions. Section 3 describes the configuration of the ESM (CESM2) employing the dust emission dataset to conduct historical simulations of the dust cycle. Section 4 introduces the CMIP6 and independent dust PM concentration data for model–observation comparisons. Section 5 discusses the evaluation of the ESM dust simulations against CMIP6 dust simulations and long-term dust observations. Section 6 provides an estimate of the globally gridded historical dust direct REs and RFs for 1851–2000. Section 7 provides a summary of this study.

## 2 Deriving a decadally varying global gridded dust emission dataset

In this section, we first describe our methodology for obtaining a globally gridded historical dust emission dataset spanning the years 1841–2000, after which we also extend this dataset until 2100 to support future scenario simulations.

### 2.1 A historical dust emission dataset

We build on our previous methodology in Kok et al. (2023; hereafter K23), which reconstructed the globally integrated atmospheric dust loading between the years 1841–2000 for each of nine major source regions. K23 did so by combining multiple sedimentary records of dust deposition (see site locations in Fig. 1; McConnell et al., 2007; Mahowald et al., 2010; Mulitza et al., 2010; Hooper and Marx, 2018; Clifford et al., 2019) with constraints on the modern-day dust deposition flux produced by each major source regions to each deposition site (Fig. 1). This allowed them to obtain the time evolution of the globally integrated deposition flux (and thus the emission flux) generated by each source region that best explained the 19 measured deposition timeseries using an inverse analysis. Below, we briefly review the methodology in K23 and then extend it to obtain a globally gridded decadal dust emission dataset.

The methodology in K23 combined the observed dust deposition time series at 19 sites (Fig. 1) with constraints on the fractional contribution that dust emissions from each source region make to the dust deposition flux at each deposition site (Eq. 2). The times series of the deposition fluxes from the core records were processed and smoothed to truncate noise and interannual variability, yielding decadally varying deposition values. Meanwhile, the constraints on the fractional contribution that dust emissions from each source region make to the dust deposition flux at each deposition site ($f_{i,j}^{cc}$) were obtained from the Dust Constraints from joint Observational-Modelling-Experimental analysis (DustCOMM) dataset

(Kok et al., 2021a, b). DustCOMM was produced by integrating an ensemble of six global aerosol model simulations with observationally informed constraints on the dust size distribution, extinction efficiency, and regional dust aerosol optical depth (DAOD) near dust source regions, providing dust reanalysis up to a particle diameter of 20 $\mu$m (dust PM$_{20}$). The DustCOMM deposition fluxes from each source region include uncertainties, which were obtained through a bootstrap procedure (Wilks, 2011) that propagates uncertainty from the spread in the model simulations, the uncertainty in observed dust abundance and microphysical properties, and the spread in the deposition flux timeseries.

Using the deposition records and the source-region resolved dust deposition constraints, K23 obtained the decadal evolution of dust cycle variables (loading, emission, and deposition fluxes) for each of the major dust source regions. They did so by assuming that the globally integrated dust variables generated by a given source region depend linearly on dust emissions from that source region. K23 then found, for each decade, the relative change $\lambda_i(d)$ in the dust deposition flux (and thus dust loading and deposition given their linear interdependency) generated by each source region $i$ that minimizes the sum of the squared differences between the deposition flux timeseries and the reconstructed dust emissions multiplied by the DustCOMM dust deposition-to-emission relationship $f_{i,j}^{cc}$. That is,

$$\chi(d)^2 = \sum_{j=1}^{N_{\text{dep}}} \left[ \sum_{i=1}^{N_{\text{sr}}} \lambda_i(d) f_{i,j}^{cc} - \beta_j(d) \right]^2, \tag{2}$$

where $\beta_j(d)$ is the measured deposition flux at site $j$ for decade $d$, normalized by its value in the last decade in the reconstructed period (1991–2000), and $\lambda_i(d)$ is the decadal dust emission flux generated by source $i$ in decade $d$, also normalized by its value in the 1990s. $N_{\text{dep}}$ = 19 is the number of deposition flux timeseries in the compilation (Fig. 1), and $N_{\text{sr}}$ = 7 is the number of dust emission source regions we defined (rectangular boxes in Fig. 1) for which we obtain reconstructed emissions $\lambda$. We note that although DustCOMM in Kok et al. (2021a) defined $N_{\text{sr}}$ = 9 sources, deposition fluxes from the three North African sources (Western and Eastern North Africa, and the Sahel) tend to be correlated. Since there are currently insufficient dust deposition records dominated by dust from the Sahel and Eastern North Africa, these three sources cannot be separately inverted robustly. Thus, in this study these three sources were grouped into one bigger region similar to the North Africa source used in Mahowald et al. (2010), yielding a total of $N_{\text{sr}}$ = 7 sources (Fig. 1). Lastly, $f_{i,j}^{cc}$ is the reanalyzed dust deposition-to-emission relationship provided by DustCOMM (from Kok et al., 2021a, b; hereafter K21), the fractional contribution of dust emissions from the $i^{\text{th}}$ source to the deposition flux at the $j^{\text{th}}$ core site in the current climate (cc) (see colors in Fig. 1). In K21, $f_{i,j}^{cc}$ is jointly determined by both meteorological factors (such as wind circulation and precipitation) and the emission strengths of the different source regions in the current climate. $f_{i,j}^{cc}$ is used to quantify the optimizable deposition flux $\hat{\beta}_j$ at the $j^{\text{th}}$ site in the $d^{\text{th}}$ decade:

$$\hat{\beta}_j(d) = \lambda_1(d) f_{1,j}^{cc} + \lambda_2(d) f_{2,j}^{cc} + \ldots + \lambda_{N_{\text{sr}}}(d) f_{N_{\text{sr}},j}^{cc} = \sum_{i=1}^{N_{\text{sr}}} \lambda_i(d) f_{i,j}^{cc} \tag{3}$$

such that the cost function in Eq. 2 can also be expressed as $\chi(d)^2 = \sum_{j=1}^{N_{\text{dep}}} \left[ \hat{\beta}_j(d) - \beta_j(d) \right]^2$. Since $f_{i,j}^{cc}$ was obtained using 2004–2008 ESM simulations and observational constraints (in K21), we here apply the stationarity assumption that $f_{i,j}^{cc}$ is roughly unchanged for 1841–2000. We performed the optimization decade by decade, using the 19 deposition time series $\beta_j$ and the fractional contribution $f_{i,j}^{cc}$ to solve for nine $\lambda$ values for all decades in 1841–2000. The seven sources together account for the vast majority of natural desert dust emissions (Kok et al., 2021a), excluding emissions from high latitudes (~2–3 % of global emissions; Bullard et al., 2016) and from anthropogenic activities like agriculture, industrial processes, and vehicular traffic on dirt roads outside of these seven sources (Kok et al., 2021a). Figure 2 shows the solutions to the inverted DustCOMMv1 regional emissions (in Tg yr$^{-1}$) for 1841–2000 in black color. A similar inverse analysis was previously performed in K21 for modern times (2004–2008) but

230   using observationally based regional DAOD values, which could be more accurate than measurements of dust deposition fluxes but only available for the past 2–3 decades.

To quantify the uncertainty of the inverted emissions $\lambda_i$, we solve Eq. 3 500 times using a bootstrap procedure (e.g., Efron, 1982; Chernick, 2007) that propagates various uncertainties in the DustCOMM dataset (e.g., uncertainties in dust optics and emitted dust size distribution; see K21a) and which uses a resampling with replacement procedure to propagate uncertainty in the dust deposition records (see details

235   in the Supplement to K23). The DustCOMM historical dust emission dataset used to drive the CESM2 simulations in this study uses the median of the probability distribution obtained from this bootstrap procedure.

240   Finally, we extend the K23 dust reconstruction by obtaining a globally gridded dust emission dataset or inventory as

$$F_{\text{EI}}(\theta, \phi, d, s) = \sum_{i=1}^{N_{\text{sr}}} \lambda_i(d) F_{\text{cc},i}(\theta, \phi, s),\tag{4}$$

where $F_{\text{cc},i}(\theta, \phi, s)$ denotes the 2004–2008 current climate dust emissions (kg m$^{-2}$ s$^{-1}$) constrained per source region $i$ by DustCOMM as a function of latitude $\theta$, longitude $\phi$, and season $s$. $F_{\text{cc},i}$ was obtained as part of the DustCOMM dataset (Kok et al., 2021a) by calibrating emissions simulated by six global aerosol models (all regridded to a horizontal resolution of 1.9°×2.5°) to observational constraints on

245   DAOD (Ridley et al., 2016). Emissions are non-zero only inside of the source $i$ and are zero elsewhere, informing the grid-by-grid spatial variability of emissions of the $i$th source. Thus, the nondimensionalized $\lambda_i(d)$ here is the weighting or importance of each source $i$ in a given decade $d$ for aggregating a global emission map $F_{\text{EI}}$ for any $d$. As a result, $F_{\text{EI}}(\theta, \phi, d, s)$ represents our final dust emission product, with a resolution of 1.9°×2.5° (see Fig. 3 for the reconstructed contemporary emissions), representing the median

250   of the bootstrapping ensemble. We call $F_{\text{EI}}$ the DustCOMM emission dataset v1 in this study, and we will evaluate its effectiveness in reproducing the observed dust trend in ESMs by forcing a CESM historical dust cycle simulation (Sect. 5).

255   We note that $F_{\text{EI}}$ is subject to several uncertainties. First, measurements of deposition fluxes and the DustCOMM constraints on $f_{i,j}^{cc}$ both carry substantial uncertainties (Avila et al., 1997; Cakmur et al., 2006; Stanelle et al., 2014; Kok et al., 2021b). We propagated these uncertainties into $F_{\text{EI}}$ using a bootstrap procedure, of which we provide 100 ensemble members (or realizations) of the derived emissions. Second, Eqs. 1 and 2 use several critical assumptions to obtain $F_{\text{EI}}$ (see a full discussion of these assumptions in K23). The most important ones include the stationarity assumptions that (i) the spatial pattern of the dust

260   deposition flux per source region has not changed across time, and that (ii) decadal trends in deposition fluxes are caused by changes in emissions instead of transport pathways / deposition processes, and the non-local assumption that (iii) dust deposited at the 19 sites originates from representative parts of major sources and is not from non-representative local sources. Errors (i) and (ii) were partially assessed by Mahowald et al. (2010), who concluded that each source's simulated transport and deposition patterns

265   changed relatively little over time. Nonetheless, considering these assumptions and the resulting systematic errors, the error estimates on our emission inventory should be considered a lower bound.
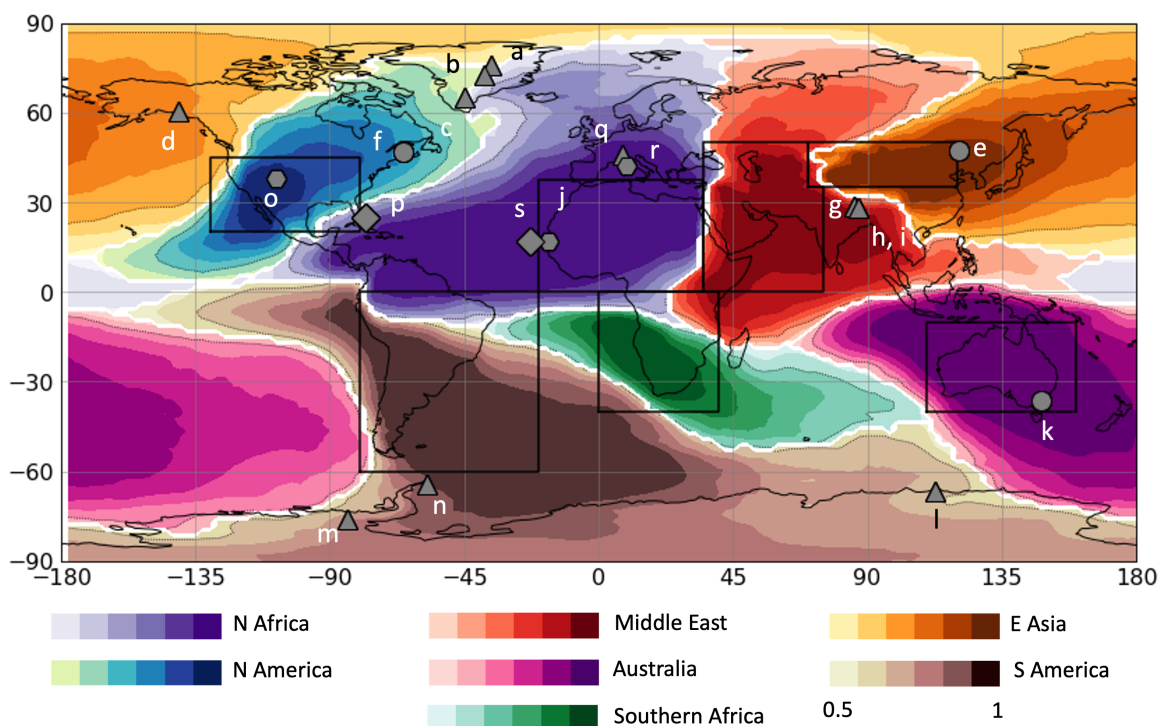
Figure 1. Map of deposition record sites and dominant dust source regions. The black boxes denote the seven major source regions (North Africa, the Middle East & Central Asia, East Asia, North America, Australia, South America, and Southern Africa). The colors represent which source region contributes the greatest deposition flux in the current climate (cc) at a given grid, with the shading denoting the fractional contribution of that dominant source region. The letters correspond to the panel of the retrieved dust deposition time series in Fig. 4. Gray symbols denote the locations of the 19 dust deposition records used to reconstruct dust loading since preindustrial times, with triangles, circles, diamonds, and hexagons respectively denoting records extracted from ice, marine/lake sediment, coral, and peat cores. The figure is replotted after Kok et al. (2021b) Fig. 8a, which was originally created by Ron L. Miller.

## 2.2 Extending the dust emission dataset into the future

In addition to obtaining an emission dataset for the historical period, we also derive emission datasets of plausible future scenarios of dust emissions. These emission datasets could be used in simulations of future climate to evaluate the effects of different reasonable assumptions about how dust emissions could evolve in the future. Currently, it is unclear whether dust emissions will increase or decrease in the future (e.g., Mahowald and Luo, 2003; Tegen et al., 2004; Achakulwisut et al., 2017; Pu and Ginoux, 2017; Li et al., 2021b; Wu et al., 2022; Liu et al., 2024), both because model projections diverge (Kok et al., 2018; Thornhill et al., 2021) and because we have insufficient mechanistic understanding of what caused the historical changes in dust emissions and how those drivers might change in the future (Ginoux et al., 2012; Kok et al., 2023). Hence, we provide three future emission scenarios that span a range of plausible possibilities. The enhancement scenario assumes that the historical dust trend will continue post-2020; the constant scenario assumes that dust emissions will remain at present day levels; and the reduction scenario assumes that the trend in dust emissions will reverse, decreasing post-2020 at the same rate it increased over the historical period. All scenarios assume that dust emissions

stayed constant for 2001–2020, which is largely consistent with what satellite data implies (Logothetis et
al., 2021).

We calculate the emissions for each decade after 2020 as follows:

$$F_{EI}(\theta, \phi, s, d) = \sum_{i=1}^{N_{sr}} [1 + f_s \eta_i d_f] F_{cc,i}(\theta, \phi, s),\qquad(5)$$

where $d_f$ is the number of decades past the 2010s (e.g., $d_f = 7$ for the 2080s), and $f_s$ is a scenario-dependent
constant that equals 1, 0, and -1 for the three scenarios with enhanced, constant, and reduced future dust,
respectively. Finally, $\eta_i$ [decade⁻¹] is the change per decade in dust emissions emitted by source region $i$,
normalized by the modern-day (1981–2000) dust emissions from that source region. We obtained $\eta_i$ from
a linear fit to the reconstructed 1841–2000 dust emissions, which yields 0.027, 0.030, 0.038, and 0.030,
0.014, 0.038, and 0, for the North Africa, Middle East & Central Asia, East Asia, North America, Australia,
South America, and South Africa source regions, respectively. Note that the South African source region
was assumed to have remained constant over 1841–2000 due to a lack of deposition data to constrain it
(see Fig. 1 and Kok et al., 2023). Figure 2 shows the regionally aggregated dust emission variability for
1841–2100 from the DustCOMMv1 dataset, comprising plots for all three future scenarios. Note that we
here focus only on evaluating the historical $F_{EI}$, and exploring dust impacts on future climate using the
future $F_{EI}$ will be the topic of future work.
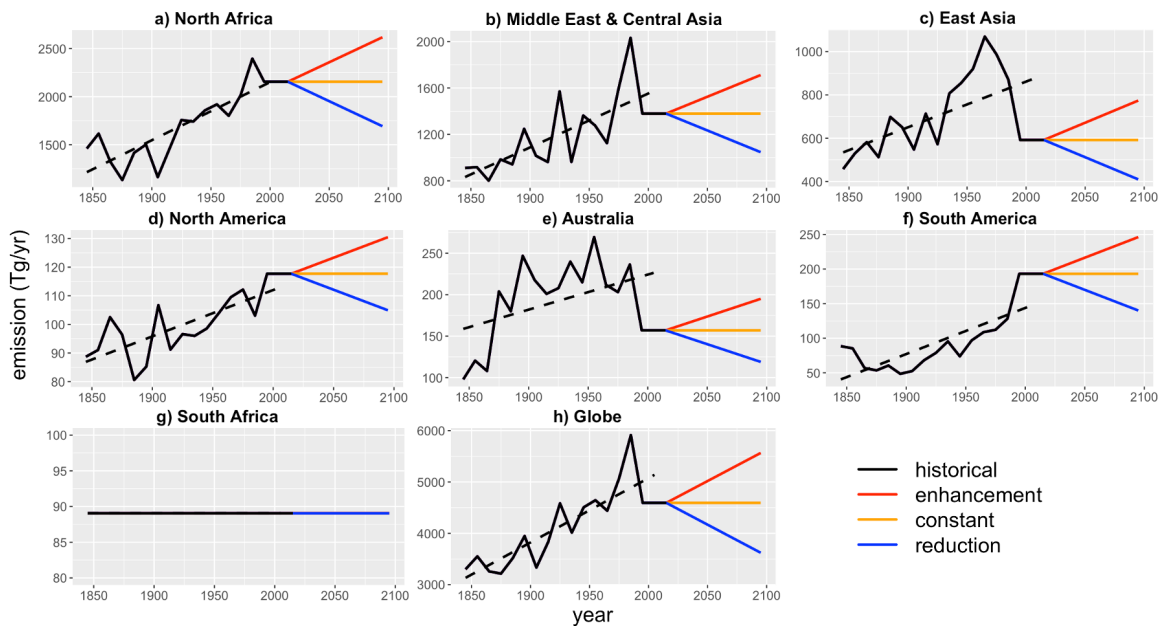
Figure 2. Decadal timeseries of the regional mean and global mean dust emissions (Tg yr⁻¹) for 1841–
2100. The black lines show the solutions of the DustCOMM (a-g) inverted emissions for the seven defined
source regions in this paper and (h) the globally aggregated emission for 1841–2000, which are evaluated
in this paper. The dashed lines show the corresponding linear trend to the 1841–2000 emissions. South
African emissions were assumed to have remained constant because there are no deposition core records
available to constrain its temporal evolution. The 2001–2020 emissions were set to remain equal to the
1991–2000 emissions, and the 2020–2100 period contains three future dust emission scenarios:

320    enhancement (red; following the same historical trend), constant (green; horizontal line), and reduction (blue; same as the historical trend with a negative sign).

## 3 Using CESM to evaluate the impact of historical DustCOMMv1 emissions

325

### 3.1 Coupled model configuration

We use the CESM version 2.2 (hereafter CESM2; Danabasoglu et al., 2020), a coupled ESM with multiple earth system components including atmosphere, land, ocean, and sea ice. We use a model configuration (FHIST) of CESM2 that couples the land model to the atmospheric model, while other

330    components (e.g., ocean, sea ice, glacier/land ice) use prescribed data (AMIP configuration). The SST and sea ice dataset is from the reconstructed historical dataset derived by the Met Office Hadley Centre (HadISST, Rayner et al., 2003). Anthropogenic and natural emissions of chemical tracers and aerosols (except dust) and land use changes evolve with time follow the CMIP6 standard forcings, based on the descriptions in Emmons et al. (2020; their Sect. 5) and Lawrence et al. (2019; their Sect. 2.3.1). Our

335    configuration uses a horizontal resolution of 0.9°×1.25°, 32 vertical levels, and a time step of 30 minutes and we ran the simulation for the period 1851–2000.

### 3.2 Land model configuration

The Community Land Model (CLM5) is the land model component of CESM2. It represents

340    multiple land processes, including surface energy fluxes, surface hydrology, and land biogeochemical cycles. We use the satellite phenology (SP) mode in CLM5, which means that vegetation state (leaf area index, canopy height, vegetation type) is prescribed . The annual LULCC in CLM5 follows the Land Use Harmonization 2 (LUH2) dataset (Hurtt et al., 2020). CLM5 contains a mechanistic dust emission module that estimates dust emission flux (kg m$^{-2}$ s$^{-1}$) as a function of meteorological and land-surface variables

345    (Leung et al., 2023, 2024). Dust emission fluxes are then passed to the atmospheric model for simulating dust transport and radiative effects.

In this study, we will compare the differences in dust cycle simulations using both the mechanistic dust emission scheme and the derived emission inventory. Instead of the default CLM5 dust emission scheme (Zender et al., 2003), we use an updated scheme based on our prior work (Leung et al., 2023;

350    hereafter the CESM2–L23 run). The L23 scheme adds or improves upon several components of dust emission physics on top of the physically based Kok et al. (2014) scheme. We showed in Leung et al. (2024) that L23 outperforms both the Kok et al. (2014) scheme and the default dust emission scheme in CLM5 (the DEAD scheme; Zender et al., 2003) in capturing the spatial and day-to-day temporal variability of atmospheric dust, but the long-term (interdecadal) temporal variability of dust was not

355    assessed. In addition, we also performed a historical simulation using the prescribed DustCOMMv1 emissions to force an observationally constrained dust trend (hereafter the CESM2–DustCOMM run). CLM5 regridded the emission data to the model resolution in both space and time. The processed emissions were then passed on to CAM6 for atmospheric dust aerosol simulations.

360    ### 3.3 Atmospheric model configuration

The Community Atmosphere Model (CAM6) takes the emission fluxes from the land model and simulates the transport, deposition, optical properties, and radiative effects of dust aerosols using a four mode aerosol model (MAM4). The four aerosol modes in MAM4 include the Aitken mode (0.01–0.1 μm), the accumulation mode (0.1–1 μm), the coarse mode (1–10 μm), and the primary carbon mode (Liu et al.,

365    2016). Dust is in all modes except the primary carbon mode. The emitted dust size distribution is based on brittle fragmentation theory (BFT; Kok, 2011), with respective contributions of 0.1 %, 1.0 %, and 98.9 % for the Aitken, accumulation, and coarse modes. The coarse mode in CAM6 includes dust up to a diameter

of ~10 $\mu$m and therefore misses the super-coarse dust ranging between 10 and 62.5 $\mu$m, which produces radiative effects in both the shortwave and the longwave spectra (Adebiyi et al., 2023).

370    CAM6 uses a tracer advection scheme to transport dust aerosols (Neale et al., 2012). Aerosols in each mode are transported as an internal mixture of the different aerosol species present, with their physical properties (e.g., optical properties and density) predicted based upon the volume fraction of each species, while aerosol species from different modes are externally mixed. CAM6 simulates the removal of aerosols via dry deposition and wet deposition. Dry deposition includes turbulent and gravitational
375    settling (Zhang et al., 2001), and wet deposition of aerosols includes in-cloud and below-cloud scavenging (Neale et al., 2012) for both stratiform and convective clouds (Shan et al., 2021).

The CAM6 radiative fluxes are computed by the Rapid Radiative Transfer Method for General Circulation Models (RRTMG; Iacono et al., 2008). RRTMG computes the net radiative flux based on the radiation diagnosed at 14 SW and 16 LW spectral bands. We note that RRTMG only accounts for
380    absorption (and not scattering) for the LW bands, while it accounts for both scattering and absorption for the SW bands (Dusfresne et al., 2002; Di Biagio et al., 2020). The dust DRE is determined by calculating the difference of the net radiative flux with and without dust at the top of the atmosphere (via a double radiation call). Dust optical properties (i.e., single scattering albedo, mass extinction efficiency, and asymmetry factor) are functions of the complex refractive index (CRI). The optical properties of the
385    internally mixed aerosols in a mode are based upon the CRI of that mixture, calculated as the volume-weighted CRI of the aerosol species as well as water (Ghan and Zaveri, 2007).

In this study, we calculate dust optical properties using the dataset of CRI in the SW spectrum from Di Biagio et al. (2019). This dataset contains the real (scattering) and imaginary (absorption) refractive indices in the SW bands (300–1100 nm) from multiple dust samples collected across the globe.
390    We take the mean CRIs (see Table 4 in Di Biagio et al., 2019) to replace the existing CAM6 dust CRIs, which are originally based on the Optical Properties of Aerosols and Clouds package (OPAC; Hess et al., 1998) and the Aerosol Robotic Network (AERONET; Dubovik et al., 2000) retrieved optical properties for the SW bands, while holding the LW CRIs unchanged (i.e., still CAM6 dust optics), since previous studies found that ESM-prescribed and AERONET optical properties are generally too absorbing (e.g., Di
395    Biagio et al., 2019; Adebiyi et al., 2023). The CAM6 and Di Biagio CRIs are summarized in Table S2. Both have similar real refractive index ($n = 1.56$ for CAM6 and $n = 1.52$ for Di Biagio for the whole visible band), but the imaginary part ($k$) is smaller in the Di Biagio optics than in CAM6 (e.g., for 300 nm, $k = –0.0052$ for CAM6 and $k = –0.0026$ for Di Biagio), implying the Di Biagio optics will yield less absorption and thus less warming by dust aerosols. We will use the Di Biagio optics for simulations and
400    results in Sect. 5.

Atmospheric dust simulations are usually tuned to match an observational constraint, such as the global mean DAOD, since there are no a priori physical principles that confine the order of magnitude of the simulated dust budget from the dust emission schemes (Leung et al., 2024). Process-based dust emission schemes can thus only simulate the spatiotemporal dust variability and then multiply the
405    emissions by a global tuning factor to scale the emissions to a global magnitude consistent with satellite and ground-based observations. In this study, we scale our simulations to have global mean DAOD values averaged across 1981–2000 to be 0.03±0.01 (95 % confidence interval), consistent with current global constraints used by CMIP6 ESMs and other previous studies (e.g., Ito et al., 2021; Klose et al., 2021; Li et al., 2022; Zhao et al., 2022).

410

## 4 Datasets used for evaluating CESM simulations using the DustCOMM emission dataset

### 4.1 Dust PM concentration records over Barbados and Miami from 1960s to 2000s

415    We use different datasets to evaluate the derived DustCOMM emissions in this stidy. Apart from the deposition fluxes from the core records, there are two long-term measurements of dust mass

concentrations at Miami (Zuidema et al., 2019) and Barbados (Prospero et al., 2021) from the 1960s to the 2000s, which we use to evaluate the CESM dust PM simulations using the DustCOMM emissions for part of the covered time period. Aerosol samples were collected daily over both sites with high-volume filter samplers. The contribution from local sources was minimized by only sampling when there were easterly winds of > 1 m s⁻¹ from the ocean.

**4.2 CMIP6 dust data for evaluation**

We also compare our dust simulations with those from multiple ESMs within the Coupled Model Intercomparison Project phase 6 (CMIP6) experiments (https://esgf-node.llnl.gov/search/cmip6/; see Table S1 for model information). We have included both the historical runs and the amip-hist runs from the CMIP6 experiment. In CMIP6, "historical" refers to runs with active atmosphere–ocean coupling, while "amip-hist" refers to runs with inactive ocean components forced with HadISST. Note that not all CMIP6 models provided the same dust cycle variables, which means that the figures in Sect. 5 that evaluate different dust variables show different models for each comparison. Most ESMs provided DAOD fields, but only a few models provided dust PM or dust deposition fields.

**5 Evaluating the new dust emission dataset in CESM2**

**5.1 Simulated dust emission and DAOD using L23 and DustCOMM emissions in CESM2**

We first compare how the simulated dust cycles evolves with time in the CESM2. Figure 3 shows the simulated dust emissions and DAOD in the CESM–L23 and the CESM2–DustCOMM runs averaged across 1981–2000 and their changes over the historical period (1981–2000 minus 1851–1860). The dust maps for the 1851–1860 periods are also shown in Fig. S1. CESM2–L23 dust emissions show a realistic global emission pattern mostly focused on Africa, the Middle East, Asia, Australia, and the Americas (Fig. 3a). In L23, total emissions changed little over the historical period (Fig. 3b), hovering around a global emission rate of ~1800 Tg yr⁻¹, although there are some regional changes in emissions. DAOD also remained almost the same, staying at a global mean of ~0.028 (Fig. 3c). Figure 3d shows the change in DAOD, indicating a slight decrease in Asia and a small increase in the Sahara. The simulated historic dust cycle trends in CESM2–L23 are small, possibly because of the insignificant historical trends of the simulated meteorological drivers (e.g., wind speed, soil moisture and leaf area index) or the insufficient simulated dust sensitivity to these drivers, as suggested by Kok et al. (2014a, 2018). This insignificant change in the simulated dust cycle is consistent with previous studies (e.g., Mahowald et al., 2010; Kok et al., 2023) showing that current ESM dust simulations generally are unable to capture the long-term increase in dust that is evident from sedimentary records of dust deposition (Fig. 4).

For the CESM2–DustCOMM run (Fig. 3e-h), Fig. 3e shows the dust emissions averaged over 1981–2000, which is essentially identical to the DustCOMM emissions read in by CLM5. The largest emissions occur over China and the Middle East (~1 kg m⁻² yr⁻¹ or more), whereas some parts of the Sahel have relatively low emissions (~0.1 kg m⁻² yr⁻¹ or less). Overall, there are fewer emissions from semiarid regions than the L23 emissions. The 1981–2000 mean DAOD (Fig. 3g) also shows that areas with the highest DAOD are the Taklamakan Desert in China, the Rub' al Khali Desert over the Arabian Peninsula, and the western Sahara. The emissions increased ~ 50 % globally relative to the 1851–1870 period (see Fig. S1), yielding a global total of 2140 Tg yr⁻¹. Emissions increased over most of the globe (Fig. 3f), but the most significant increase in magnitude is over the Arabian Peninsula. Global DAOD (Fig. 3h) also increased by ~52 % from 0.022 (Fig. S1d) in 1851–1870 to 0.034 in the 1981–2000 (Fig. 3h). We thus successfully generated ~50 % more dust in the CESM2 throughout the historical period using the DustCOMM emissions.
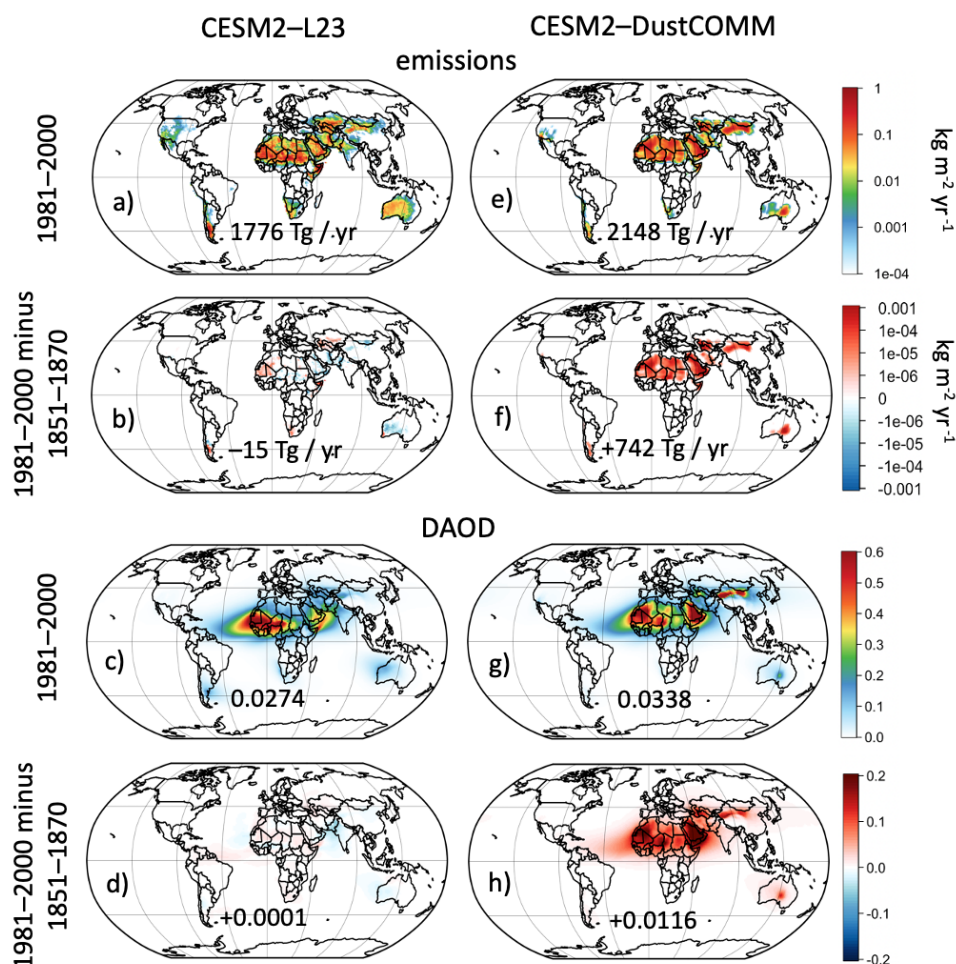
Figure 3. The CESM2 dust cycle simulation using the Leung et al. (2023; L23) dust emission scheme and the DustCOMM globally gridded emission dataset v1 derived in this study. (a-d) The CESM2–L23 simulated maps averaged across 1981–2000, as well as the difference between the 1981–2000 and 1851–1870 periods, for both (a, b) dust emissions and (c, d) dust AOD. (e-h) Same maps showing the historical dust increase, but for the CESM2–DustCOMM run. The 1851–1870 dust emission and DAOD maps are also shown in Fig. S1.

## 5.2 Model–observation comparison of dust deposition flux

Next, we examine our simulated CESM2 dust cycle as well as those from the CMIP6 dust simulations to assess whether ESM simulations capture the historical interdecadal dust variability as exhibited in the sedimentary records. To do this, we extract the 1851–2000 dust deposition fluxes over the 19 grid cells containing the core sites from all ESM simulations, including the CESM2–L23 run, the CESM2–DustCOMM run, and several CMIP6 ESMs that reported dust deposition fluxes as an output. To focus on the variability instead of the magnitude, we take the decadal median values from the annual mean deposition time series and normalize all median time series by their respective values for the period 1851–

485     1860. All time series in Fig. 4 thus have a value of zero during the 1850s. Table S3 summarizes the temporal correlation coefficients of deposition fluxes between the core records and our two CESM2 runs for 1851–2000 over the 19 site locations.

We first discuss the historical temporal variability of the measured dust deposition fluxes (black lines) in Fig. 4. Most observed deposition fluxes (black lines) exhibit a rising trend (e.g., in Fig. 4e–j),
490     with many showing increases of more than 100% across 1850–2000 (e.g., Fig. 4c–f). Some observed deposition flux time series exhibit strong interdecadal variability but no secular trends (Fig. 4a–b, l). Those locations are typically near the margins of control between several sources, as shown by the color contours $f_{i,j}^{cc}$ in Fig. 1. For instance, NEGIS and GISP2 (Fig. 4a–b) are located near the margins of control between North America, North Africa, and East Asia (see Fig. 1), and their interdecadal variability might have
495     been jointly or alternately controlled by the three sources across time. Meanwhile, some deposition fluxes exhibit different variability despite being dominated by the same source region or even being adjacent to each other (e.g., the Lake Bastani deposition flux in Fig. 4r shows little variability while the Colle Gnifetti timeseries in Fig. 4q shows a strong trend). This indicates that deposition fluxes are affected by large experimental errors (e.g., Avila et al., 1997) and/or have large spatial variability on the length scale of a
500     model gridbox, inducing representation errors when used to inform climate model simulations (Schutgens et al., 2017).

We then examine how well different ESMs can reproduce the interdecadal variability of the measured dust deposition fluxes. In Fig. 4, the CESM2–L23 run (blue solid lines) and the historical CMIP6 runs (colored dashed lines), which use mechanistic emission schemes, generally cannot replicate the dust
505     trend over most of those sites. Our CESM2–L23 run shows distinct dust variability from the CESM2– DustCOMM run (red solid lines) despite using the same land and atmosphere model configurations. CMIP6 simulations also mostly have insignificant correlations with the observed deposition fluxes. This shows that ESMs cannot dynamically simulate the historically strengthening dust cycle.

The CESM2–DustCOMM run generally replicates the decadal deposition variability best out of
510     all ESMs simulations in Fig. 4, showing increasing deposition fluxes at most cores. However, not all simulated deposition fluxes match well the measured deposition timeseries. Although the measured dust increases are matched well over some sites (e.g., Fig. 4n and s) that are typically closer to the defined source regions, the increasing rates are underestimated over sites (e.g., Fig. 4c, e, f, j) further away from the sources, likely because different core sites contain different dust trends although dominated by the
515     same source. Thus, each source's optimized interdecadal dust emission (and hence dust deposition) trend will be intermediate between that of the relevant sites, resulting in a relatively benign dust trend than sites with stronger rising trends. Furthermore, ESMs all have different $f_{i,j}^{cc}$ values than the DustCOMM-derived $f_{i,j}^{cc}$, likely augmenting the discrepancies. Overall, for sites that give clear increasing deposition trends (Fig. 4c, j, q, and s), the CESM2–DustCOMM run yields high correlations ($r = 0.7$–$0.9$) with the observed
520     deposition fluxes. For certain sites without long-term trends but with substantial interdecadal variability (Fig. 4h–i, k), the CESM2–DustCOMM run also successfully captures their variability, although sometimes the magnitude could be less pronounced (e.g., the Snowy Mountain in Fig. 4k).

The CESM2–DustCOMM run does fail to capture the measured deposition variability at some sites (e.g., Fig. 4a–b, d, l), which are usually co-determined by two or more source regions (Fig. 1) such
525     that ESMs might not be able to simulate the same $f_{i,j}$ as reality. In addition, these marginal sites may contain some dust from high-latitude sources (Bory et al., 2003; Groot Zwaaftink et al., 2016), which is not accounted for by the prescribed emissions. For example, observed dust in NEGIS and GISP2 (Fig. 4a-b) in Greenland exhibit only pronounced interdecadal variability, which differs from the increasing trend predicted by the CESM2–DustCOMM run.

530     The CESM2–DustCOMM run also could not match the observed deposition flux from sites with little or no variability (e.g., Fig. 4o, p, r) although these sites are well within the source regions. For instance, Andros Island (Fig. 4p) and Lake Bastani (Fig. 4r) show different dust variability from other

neighboring sites affected by North African dust, which is surprising since Lake Bastani is adjacent to
Colle Gnifetti (Fig. 4q) with strong dust variability. Also, dust at San Juan Lakes (Fig. 4o) unexpectedly
535 exhibits little influence from the Dust Bowl during the 1930s. Since sites with little observed deposition
variability have smaller influences on the inversion process, the derived emissions can hardly replicate the
observed dust variability over those sites, resulting in the correlations between simulated and measured
dust ranging from –0.2 to –0.5.

We summarize the correlations between simulated and measured deposition fluxes over the 19
540 sites in Fig. 5 and Table S3 as boxplots. The CESM2–DustCOMM run yields a median correlation of 0.55,
which is substantially higher than that of other simulations. The CESM2–L23 run and other ESM
simulations have averaged correlations close to zero, although the CMIP6 multimodel ensemble run
(median = 0.18) performs better than the individual CMIP6 ESMs.

545
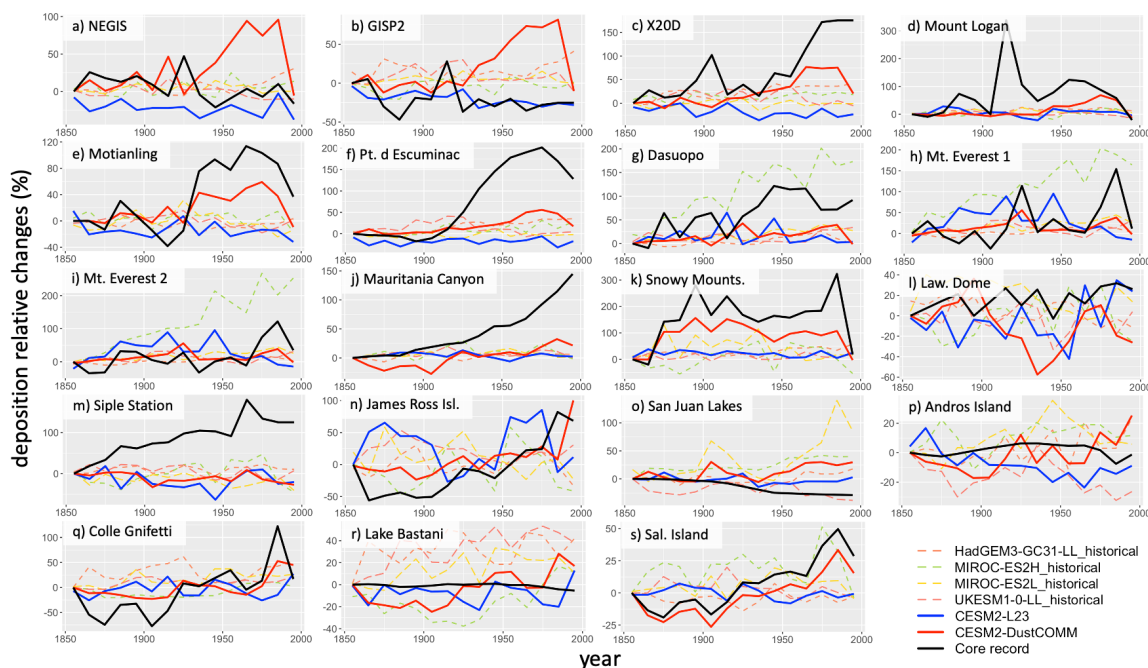
Figure 4. Comparisons between ESM simulations and measured deposition flux timeseries from
sedimentary cores. The panel letters correspond to the letters of the 19 individual sedimentary site
locations as shown in Fig. 1. The black lines show the deposition flux time series, the blue lines show our
550 CESM2 run using a mechanistic dust emission scheme (Leung et al., 2023; CESM2–L23), and the red
lines show our CESM2 run forced by the new DustCOMM emission inventory (CESM2–DustCOMM).
Colored dashed lines show the CMIP6 ESM simulated dust deposition fluxes. For ESM deposition fluxes,
we perform the comparison using the deposition time series from the grids that contain the core site
locations.

555
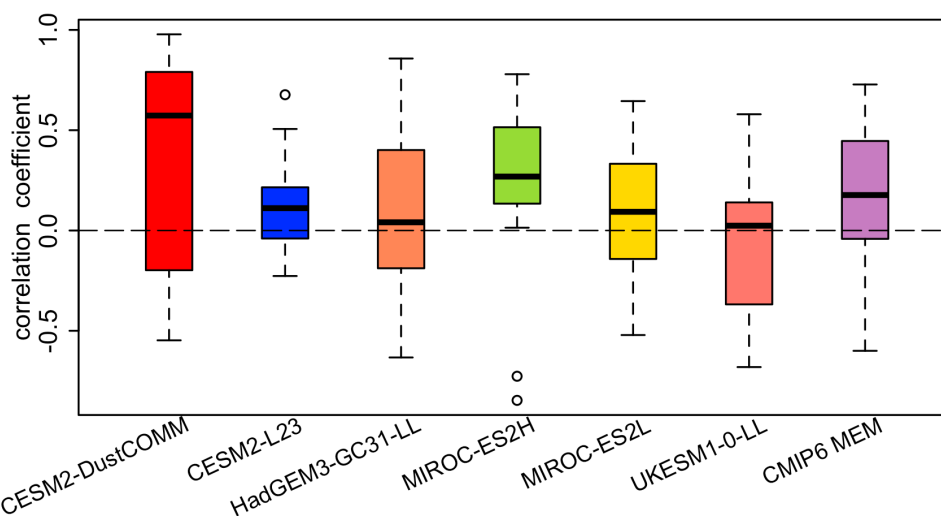
Figure 5. A boxplot summary of the correlations between the measured deposition flux time series and the deposition flux time series simulated by our runs and the CMIP6 historical runs. This figure summarizes the computed correlations between the black line and the colored lines in Fig. 4. The CMIP6 multimodel ensemble (MME) gives the mean of the four CMIP6 models that provided dust deposition fields.

## 5.3 Model–observation comparison of dust PM concentration

In another evaluation of the DustCOMM emission dataset, we compare in Fig. 6 the decadal variability of the simulated surface dust PM concentrations ($\mu g\ m^{-3}$) against long-term measurements of dust concentration at the Miami and Barbados sites (Zuidema et al., 2019; Prospero et al., 2021; see Section 4.2). For comparison of these record against ESM simulations, we use te simulated dust concentration at the gridboxes that contain the site location. Because we again focus on the interdecadal variability, we assess measured and modeled relative changes in decadally averaged values.

The dust concentration time series at the Miami site (Fig. 6a) and the Barbados site (Fig. 6b) show that dust concentrations (black lines) peaked during the 1981–1990 decade, consistent with the 1980s dust peak shown by the dust reconstruction in K23 (see the black line in Fig. 7). However, the CESM2–L23 concentration time series (blue lines) shows little decadal variability. Similarly, both the CMIP6 coupled historical runs and amip-hist runs are unable to reproduce the variability of long-term dust concentration measurements. This shows that the current generation of ESMs that employ mechanistic dust emission schemes cannot simulate the historical interdecadal variability of dust. In contrast, the CESM2–DustCOMM dust concentration (red lines) increased from the 1960s to the 1980s, peaked in the 1980s, and dropped during the 1990s, showing more consistency with the measurements. Figure 6 thus further indicates that ESMs using the DustCOMM emissions can better simulate the temporal dust variability than using mechanistic emission schemes.
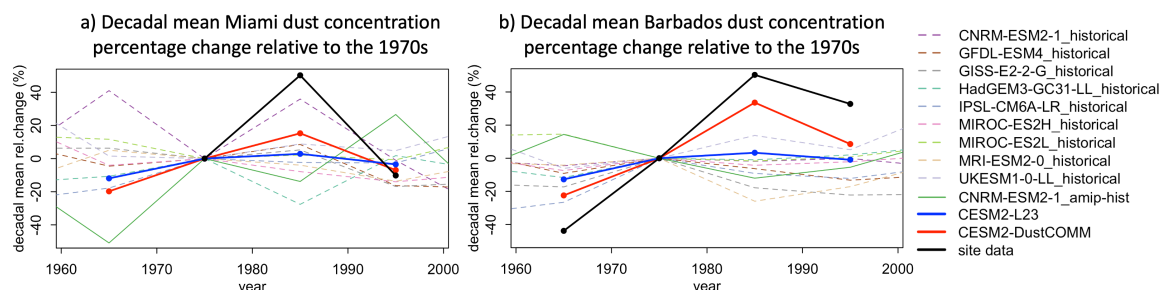
Figure 6. Measured and simulated dust PM concentrations over (a) Miami and (b) Barbados. The thick black lines show the measured dust concentrations over the two locations (Zuidema et al., 2019; Prospero et al., 2021), and the thick blue and red lines show our CESM2 simulations. The thin dashed lines are fully coupled historical simulations performed by CMIP6 ESMs. The thin solid lines show amip-hist ESM simulations with prescribed historical SST. All time series are normalized by dividing their values by their 1971–1980 mean values.

## 5.4 Model–observation comparison of global DAOD

Finally, we examine the historical evolution of simulated DAOD in Fig. 7 below. Here we compute the 10-year running mean for all dust time series. Furthermore, we focus on the variability of dust instead of its absolute magnitude, since the global mean of dust could always be tuned and rescaled with a global tuning factor to match the observed dust budgets (Zender et al., 2003; Mahowald et al., 2010; Li et al., 2021; Leung et al., 2023). We subtract the DAOD time series by their own decadal 1851–1860 averages, then divide the time series by the same reference values. Figure 7 shows the relative changes of the 10-year running mean DAOD for our simulations and the CMIP6 simulations. The dashed lines show the CMIP6 models with historical simulations, whereas the solid lines show ESMs driven by the prescribed SST.  Most CMIP6 models show moderate interdecadal variability, but there are no significant increasing dust trends for both historical and amip-hist runs, meaning that the observed dust trends cannot be reproduced with current models using either simulated or reconstructed historical SSTs. The CESM2–L23 dust time series (solid blue) also has no significant increasing trend and only contains modest interdecadal variability. Only the CESM2–DustCOMM run generates the historical increasing dust trend highly consistent with the sedimentary records. The decadal variability in the CESM2–DustCOMM time series is consistent with that in the dust reconstruction, with a ~50 % increase in dust from 1851–1870 to 1981–2000, peaking in the 1980s. Using the prescribed emission dataset is thus likely more accurate for simulating the historical RFs of dust than using mechanistic emission schemes, provided that the spatial variability and microphysics (size distribution and optical properties) of dust are sufficiently accurate in ESMs.
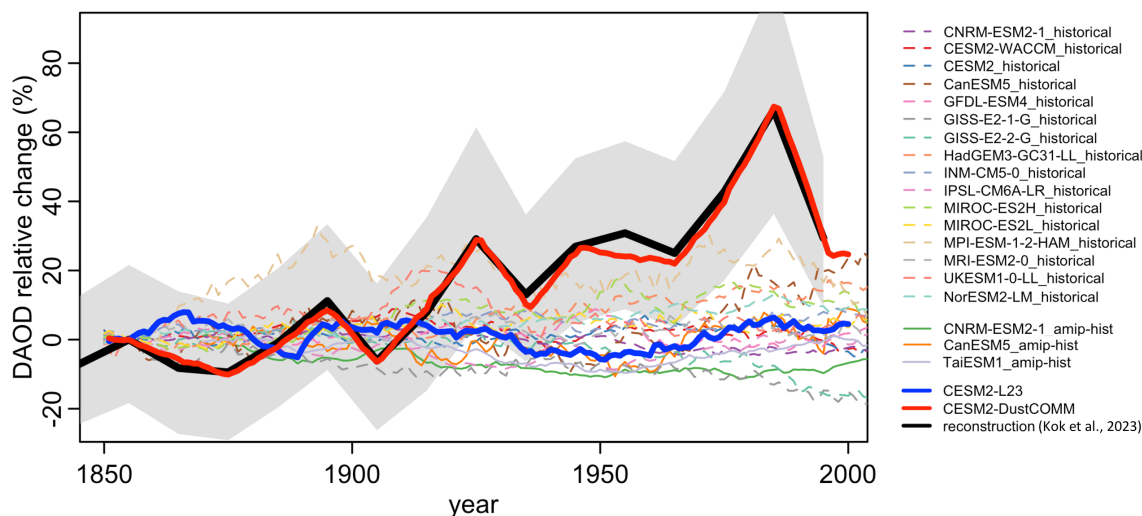
Figure 7. Changes in global dust aerosol optical depth (DAOD) relative to the 1850s/1870s. The thick solid blue and red lines show our CESM2 simulations using the Leung et al. (2023; L23) emission scheme and using the derived DustCOMM emission dataset, respectively. The thin dashed and solid lines show the CMIP6 fully coupled historical run and amip-hist runs using simulated and reconstructed historical SSTs, respectively. All the model time series are the 10-year running means from the original annual time series. The time series from the CMIP6 historical runs and our CESM runs are centered at their 1850s mean values; the DAOD time series from the amip-hist runs are centered at their 1870s means since amip-hist runs start from 1870. The solid black line shows the reconstructed DAOD time series centered at its 1850s value, and the grey shading denotes the one standard error (68% confidence) range.

## 6 Dust historical direct radiative effects and forcings in CESM2 runs

The above results show that ESMs using the derived historical emissions can produce dust cycle simulations that are more consistent with trends shown in sedimentary records of dust deposition. We then use the CESM2 to simulate the radiative effects and forcings of dust. Figure 8 shows the simulated DREs and DRFs of dust $PM_{10}$ for the two runs. We first discuss the simulated DREs for the CESM2–L23 run, in which dust remained approximately constant over time (Fig. 7). The 1851–1870 dust DRE (Fig. 8a) is large over areas where the DAOD is high (in Fig. S1b), as expected. Most of the globe exhibits negative DRE values, primarily because of dust scattering SW radiation back to space. Dust also absorbs LW radiation, but the overall warming effect is relatively weak. The only areas with positive DRE values are the most prominent dust sources (e.g., the Bodélé Depression, El Djouf, and the Rub' al Khali Desert) as they already have very high land-surface albedo for reflecting SW radiation, mitigating the SW cooling of dust aloft (e.g., Liao and Seinfeld, 1998). The late 20th century dust DRE (Fig. 8b) shows a very similar pattern as in the preindustrial period, as we would expect due to the lack of a clear dust emissions trends.

For the CESM2–L23 run, dust in the mid-19th century produced an overall global cooling effect of ∼ –0.35 W m$^{-2}$ when summing both the SW and the LW DREs. In the 1990s, the global mean dust DRE was –0.33 W m$^{-2}$, slightly smaller than the global mean dust DRE for 1851–1870. This cooling effect is in agreement with other previous CESM studies using the original CAM dust optics (e.g., Ke et al., 2021;

Li et al., 2021) and overall consistent with other modeling studies (e.g., Tegen and Lacis, 1996; Sokolik and Toon, 1996; Mahowald et al., 2010; Kok et al., 2023). The number is more negative than the $-0.15 \pm 0.35$ W m$^{-2}$ estimated by Kok et al. (2023) for the present-day dust DRE, likely because they accounted
655      for super-coarse dust (which net warms; Adebiyi and Kok, 2020) and for the warming due to LW scattering. The small change in the DRE throughout 1851–2000 is also consistent with the small decrease in the simulated historical DAOD change in Fig. 3.

     When dust emissions are prescribed (the CESM2–DustCOMM run), the magnitude of the dust DRE increased substantially across 1851–2000 (Fig. 8d-e). The DRE spatial distributions are overall
660      similar to those of the L23 run. The dust cooling effect still dominates, giving a global mean DRE of $-0.27$ W m$^{-2}$ for 1851–1870. Given the ~55 % increase in the historical dust, the global DRE increases to $-0.38$ W m$^{-2}$ for 1981–2000, giving a 41 % increase in cooling. The DRE does not necessarily need to increase by also 55 %, since DAOD increases over different geographical locations with different surface albedo values, causing warming and cooling across different regions. Furthermore, DRE is not directly
665      proportional to AOD due to multiple scattering (e.g., Di Biagio et al., 2020).

     We finally discuss the simulated historical direct RF (Fig. 8c and f), which is equal to the 1981–2000 DRE minus 1851–1870 DRE for both runs. For the CESM2–L23 run (Fig. 8c), since the global DAOD slightly changed by < 1% from 1851–1870 to 1981–2000 (Fig. 3), the dust DRF is also small (+0.019 W m$^{-2}$). The spatial pattern of the dust DRF in Fig. 8c is consistent with that of the map of DAOD
670      changes in Fig. 3d but opposite in sign. For the CESM2–DustCOMM run (Fig. 8f), its spatial pattern is very similar to its two DRE patterns (Fig. 7b and d). The global mean historical DRF is $-0.103$ W m$^{-2}$, within the range of values predicted by previous studies. For instance, Mahowald et al. (2010) predicted a 1905–1999 historical dust DRF of $-0.07$ W m$^{-2}$, Stanelle et al. (2014) predicted an 1885–2010 historical forcing of $-0.14$ W m$^{-2}$ (clear-sky condition), and Kok et al. (2023) estimated an 1841–2000 DRF of $-$
675      0.08 W m$^{-2}$. Our value could be more accurate than previous work for PM$_{10}$ dust since we use observationally based refractive indices from Di Biagio et al. (2019) and because the prescribed DustCOMM emissions could more accurately account for regional historical dust changes.
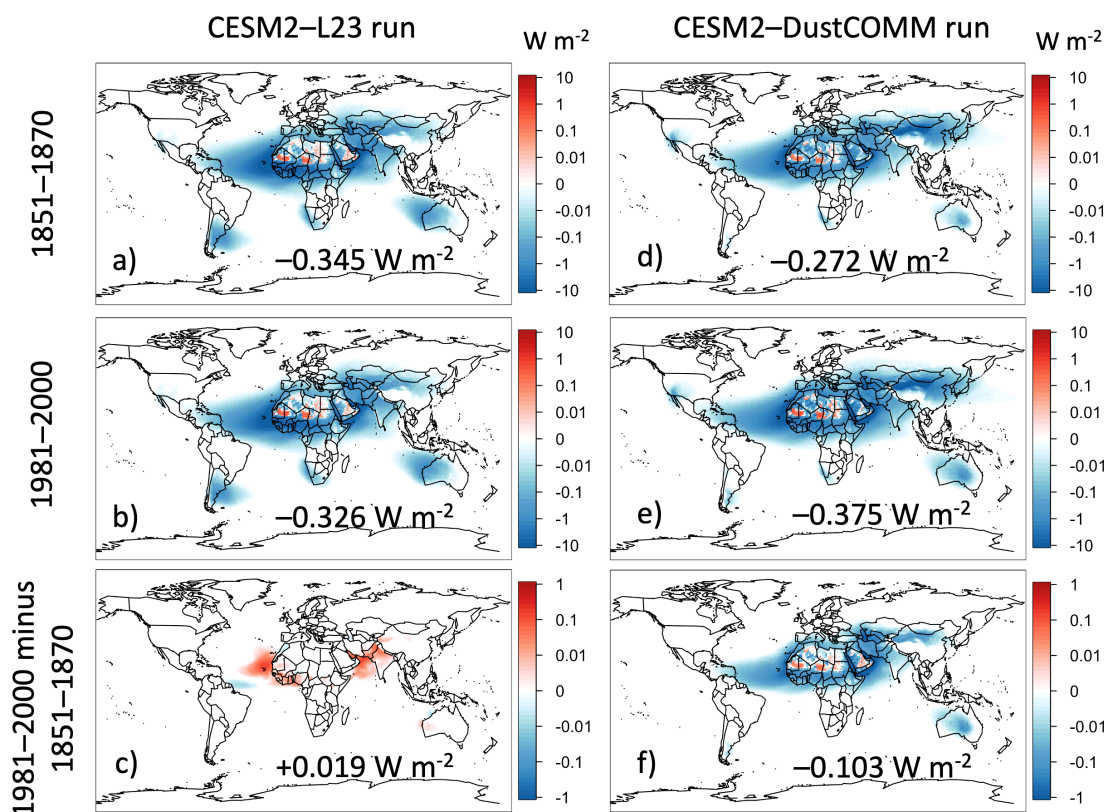
680 Figure 8. Dust direct radiative effects (DREs) and forcings (DRFs) simulated using the Leung et al. (2023;
L23) emission scheme (left columns) and the new DustCOMM emission dataset (right columns). (a-c)
CESM simulated dust DREs using the L23 emission scheme averaged across (a) 1851–1870 and (b) 1981–
2000, and (c) the 1981–2000 DRE minus 1851–1870 DRE, which equals the dust DRF for the historical
period. (d-f) As for panels (a-c) but for the CESM simulation using the DustCOMM emissions.

685

    Although we have successfully used the dust reconstruction to more realistically estimate the DRF
due to the historical dust increase, this estimation is subject to several uncertainties and limitations. First,
690 the estimated DRF is sensitive to the assumed emitted dust PSD, which is based on the brittle
fragmentation theory in the CESM2 (BFT; Kok, 2011; Li et al., 2022). Although BFT produces a dust
PSD that is in good agreement with measurements for fine and coarse dust ($D_{ve}$ < 10 μm), CESM itself
does not simulate super-coarse dust, limiting the realistic representation of the dust PSD in CESM2.
Previous studies indicated that super-coarse dust accounts for 38 (± 15%) of total atmospheric dust mass
695 (Kok et al., 2021a; Adebiyi et al., 2023). Because super-coarse dust tends to warm by absorbing SW
radiation and both scattering and absorbing LW radiation (Adebiyi and Kok, 2020), neglecting super-
coarse dust might overestimate dust radiative cooling by ~0.05–0.10 W m⁻² (Adebiyi et al., 2023). Thus,
improving the emitted dust PSD in ESMs by including dust up to ~ 50 μm in size is preferred for
adequately representing the dust DRE and DRF. Second, although we used global dust refractive indices
700 based on recent laboratory measurements (from Di Biagio et al., 2019), the amount of absorption, and thus
warming, produced by dust in the SW spectrum is uncertain (Li et al., 2021; Adebiyi et al., 2023).

Moreover, dust CRI could change based on dust source region (Di Biagio et al., 2019), which indicates spatially varying optical properties of dust aerosols (e.g., Journet et al., 2014; Green et al., 2020; Li et al., 2021a). The use of spatially varying dust optics in ESMs, or optics as a function of mineral dust species,

705   can thus further improve DRE and DRF predictions. Third, as mentioned above, the RRTMG in ESM simulations, including ours, do not include LW scattering by aerosols, which accounts for ~half of the warming from dust interactions with LW radiation (Dufresne et al., 2002; Di Biagio et al., 2020). This might possibly be overcome by employing newer radiative transfer models in CESM2 in the future (e.g., RTE+RRTMGP; Pincus et al., 2019).

710      To better evaluate the historical dust RFs and climate impacts due to historical dust changes, we recently initiated a new dust modeling intercomparison project, namely "dust radiative forcing from reconstructed dust changes since preindustrial times" (DURF), as part of the AeroCom phase III experiments. Employing multiple ESMs, dust modelers will use the DustCOMMv1 emission dataset obtained here to estimate more realistic historical dust REs and RFs.

715

## 7 Conclusions

In this study, we have derived a gridded 1841–2000 dust emission dataset (DustCOMM emissions

720   v1) using an inverse analysis for driving historical dust cycle simulations in ESMs. We did so by combining 19 sedimentary records of dust deposition for 1841–2000 across the globe with observational and modeling constraints on the present-day dust cycle to infer the changes in dust emissions for each of seven major source regions (Sect. 2). This DustCOMM emission dataset contains decadal variability of historical dust as inferred from the dust sedimentary records. It's important to note that the DustCOMM

725   emissions required important assumptions to derive (see Section 2) and that it could be subject to systematic errors, and the deposition fluxes from core records also contain large uncertainties. Therefore, more dust deposition timeseries that resolve the preindustrial-to-modern time period are urgently needed to better constrain the historical evolution of the global dust cycle. We provided 100 realizations of the historical dust emissions to characterize the uncertainties of the DustCOMMv1 emissions.

730      To evaluate the derived dataset, we used the derived emissions to drive an 1851–2000 historical dust cycle simulation in the CESM2. The simulation results revealed that the simulated dust cycle captured the historical increasing dust trend. The simulated trends in dust deposition matched moderately well against the sedimentary records and the simulated dust PM concentrations were in reasonable agreement with long-term measurements of dust concentration over Miami and Barbados. In contrast, CESM2 and

735   other ESMs employing process-based dust emission schemes showed little or no long-term increase in dust across 1851–2000. A modeling development study on enabling process-based models to capture the historical dust trend will be the topic of a future paper.

Here we showed that ESMs using our derived emissions can reproduce the observed historical dust increase and thus can better estimate the radiative forcing (RF) due to this dust increase. CESM2 using

740   prescribed DustCOMM emissions yielded an 1851–2000 dust direct RF of –0.10 W m$^{-2}$ (cooling), primarily due to scattering of shortwave radiation back to space, especially over the oceans. This value is consistent with the calculations in previous studies (e.g., Mahowald et al., 2010; Stanelle et al., 2014; Kok et al., 2023). These results suggest that historical dust changes have likely partially counteracted the historical global warming caused by the anthropogenic increase in greenhouse gases.

745

**Acknowledgements**

750 This material is based upon work supported by the NSF National Center for Atmospheric Research (NCAR), which is a major facility sponsored by the U.S. National Science Foundation under Cooperative Agreement No. 1852977. Computing and data storage resources, including the Cheyenne supercomputer (https://doi.org/10.5065/D6RX99HX), were provided by the Computational and Information Systems Laboratory (CISL) at the NSF NCAR. Danny M. Leung thank Charles G. Bardeen and Francis V. Fitt for

755 the valuable discussions on the CESM2 radiation scheme. Figure 1 in this paper was plotted after Kok et al. (2021b) Fig. 8a, which was originally created by Ron L. Miller.

**Financial Support**

760 Danny M. Leung and Jasper F. Kok are funded by the National Science Foundation (NSF) Directorate for Geosciences grants 1856389 and 2151093. Danny M. Leung completed this work while holding the NSF NCAR Advanced Study Program (ASP) Postdoctoral Fellowship. Longlei Li and Natalie M. Mahowald acknowledge support from the Department of Energy (DOE) DE-SC0021302 and the Earth Surface Mineral Dust Source Investigation (EMIT), a NASA Earth Ventures-Instrument (EVI-4) Mission.
765

**Author Contributions**

JFK and DMLe conceptualized the study. DMLe performed the model development, conducted the simulations, analyzed the simulation results, and conducted the evaluations. DMLe wrote the original manuscript and plotted all figures under JFK's supervision. LL, ST, DMLa, NMM, and EK assisted the
770 conceptualization and model development. All authors contributed to the manuscript preparation, discussion, and writing.

**Data and Code Availability**

The DustCOMM emission v1 dataset, the ensemble members of the DustCOMMv1 emissions, and the
775 processed sedimentary and ice core data of dust deposition fluxes are available on https://drive.google.com/drive/folders/1PjFISy4XEOMA0ahucYLHlQ7tb6_36boj?usp=sharing. The CESM2.2 code for reading in the DustCOMM emission dataset is also available in the same link.

**Competing Interests**
780 One of the coauthors is a member of the editorial board of Atmospheric Chemistry and Physics.

## References

785 Achakulwisut, P., Shen, L., and Mickley, L. J.: What Controls Springtime Fine Dust Variability in the Western United States? Investigating the 2002–2015 Increase in Fine Dust in the U.S. Southwest, Journal of Geophysical Research: Atmospheres, 122, 12,449-12,467, https://doi.org/10.1002/2017JD027208, 2017.

Adebiyi, A., Kok, J. F., Murray, B. J., Ryder, C. L., Stuut, J.-B. W., Kahn, R. A., Knippertz, P., Formenti, P., Mahowald, N. M., Pérez García-Pando, C., Klose, M., Ansmann, A., Samset, B. H., Ito, 790 A., Balkanski, Y., Di Biagio, C., Romanias, M. N., Huang, Y., and Meng, J.: A review of coarse mineral dust in the Earth system, Aeolian Research, 60, 100849, https://doi.org/10.1016/j.aeolia.2022.100849, 2023.

Adebiyi, A. A. and Kok, J. F.: Climate models miss most of the coarse dust in the atmosphere, Science Advances, 6, eaaz9507, https://doi.org/10.1126/sciadv.aaz9507, 2020.

795 Andreae, M. O., Jones, C. D., and Cox, P. M.: Strong present-day aerosol cooling implies a hot future, Nature, 435, 1187–1190, https://doi.org/10.1038/nature03671, 2005.

Avila, A., Queralt-Mitjans, I., and Alarcón, M.: Mineralogical composition of African dust delivered by red rains over northeastern Spain, Journal of Geophysical Research: Atmospheres, 102, 21977–21996, https://doi.org/10.1029/97JD00485, 1997.

800 Bellouin, N., Quaas, J., Gryspeerdt, E., Kinne, S., Stier, P., Watson-Parris, D., Boucher, O., Carslaw, K. S., Christensen, M., Daniau, A.-L., Dufresne, J.-L., Feingold, G., Fiedler, S., Forster, P., Gettelman, A., Haywood, J. M., Lohmann, U., Malavelle, F., Mauritsen, T., McCoy, D. T., Myhre, G., Mülmenstädt, J., Neubauer, D., Possner, A., Rugenstein, M., Sato, Y., Schulz, M., Schwartz, S. E., Sourdeval, O., Storelvmo, T., Toll, V., Winker, D., and Stevens, B.: Bounding Global Aerosol Radiative Forcing of 805 Climate Change, Reviews of Geophysics, 58, e2019RG000660, https://doi.org/10.1029/2019RG000660, 2020.

Bory, A. J.-M., Biscaye, P. E., Piotrowski, A. M., and Steffensen, J. P.: Regional variability of ice core dust composition and provenance in Greenland, Geochemistry, Geophysics, Geosystems, 4, https://doi.org/10.1029/2003GC000627, 2003.

810 Boucher, O., Randall, D., Artaxo, P., Bretherton, C., Feingold, G., Forster, P., Kerminen, V., Kondo, Y., Liao, H., and Lohmann, U.: Climate change 2013: the physical science basis. Contribution of Working Group I to the Fifth Assessment Report of the Intergovernmental Panel on Climate Change, K., Tignor, M., Allen, SK, Boschung, J., Nauels, A., Xia, Y., Bex, V., and Midgley, PM, Cambridge University Press, Cambridge, UK, 2013.

815 Bullard, J. E., Baddock, M., Bradwell, T., Crusius, J., Darlington, E., Gaiero, D., Gassó, S., Gisladottir, G., Hodgkins, R., McCulloch, R., McKenna-Neuman, C., Mockford, T., Stewart, H., and Thorsteinsson, T.: High-latitude dust in the Earth system, Reviews of Geophysics, 54, 447–485, https://doi.org/10.1002/2016RG000518, 2016.

Cakmur, R. V., Miller, R. L., Perlwitz, J., Geogdzhayev, I. V., Ginoux, P., Koch, D., Kohfeld, K. E., 820 Tegen, I., and Zender, C. S.: Constraining the magnitude of the global dust cycle by minimizing the

difference between a model and observations, Journal of Geophysical Research: Atmospheres, 111, https://doi.org/10.1029/2005JD005791, 2006.

Chernick, M. R.: Bootstrap Methods: A Guide for Practitioners and Researchers, 2007.

825   Clifford, H. M., Spaulding, N. E., Kurbatov, A. V., More, A., Korotkikh, E. V., Sneed, S. B., Handley, M., Maasch, K. A., Loveluck, C. P., Chaplin, J., McCormick, M., and Mayewski, P. A.: A 2000 Year Saharan Dust Event Proxy Record from an Ice Core in the European Alps, Journal of Geophysical Research: Atmospheres, 124, 12882–12900, https://doi.org/10.1029/2019JD030725, 2019.

Danabasoglu, G., Lamarque, J.-F., Bacmeister, J., Bailey, D. A., DuVivier, A. K., Edwards, J., Emmons, L. K., Fasullo, J., Garcia, R., Gettelman, A., Hannay, C., Holland, M. M., Large, W. G., Lauritzen, P.
830   H., Lawrence, D. M., Lenaerts, J. T. M., Lindsay, K., Lipscomb, W. H., Mills, M. J., Neale, R., Oleson, K. W., Otto-Bliesner, B., Phillips, A. S., Sacks, W., Tilmes, S., van Kampenhout, L., Vertenstein, M., Bertini, A., Dennis, J., Deser, C., Fischer, C., Fox-Kemper, B., Kay, J. E., Kinnison, D., Kushner, P. J., Larson, V. E., Long, M. C., Mickelson, S., Moore, J. K., Nienhouse, E., Polvani, L., Rasch, P. J., and Strand, W. G.: The Community Earth System Model Version 2 (CESM2), Journal of Advances in
835   Modeling Earth Systems, 12, e2019MS001916, https://doi.org/10.1029/2019MS001916, 2020.

Di Biagio, C., Formenti, P., Balkanski, Y., Caponi, L., Cazaunau, M., Pangui, E., Journet, E., Nowak, S., Andreae, M. O., Kandler, K., Saeed, T., Piketh, S., Seibert, D., Williams, E., and Doussin, J.-F.: Complex refractive indices and single-scattering albedo of global dust aerosols in the shortwave spectrum and relationship to size and iron content, Atmospheric Chemistry and Physics, 19, 15503–
840   15531, https://doi.org/10.5194/acp-19-15503-2019, 2019.

Di Biagio, C., Balkanski, Y., Albani, S., Boucher, O., and Formenti, P.: Direct Radiative Effect by Mineral Dust Aerosols Constrained by New Microphysical and Spectral Optical Data, Geophysical Research Letters, 47, e2019GL086186, https://doi.org/10.1029/2019GL086186, 2020.

Dubovik, O., Smirnov, A., Holben, B. N., King, M. D., Kaufman, Y. J., Eck, T. F., and Slutsker, I.:
845   Accuracy assessments of aerosol optical properties retrieved from Aerosol Robotic Network (AERONET) Sun and sky radiance measurements, Journal of Geophysical Research: Atmospheres, 105, 9791–9806, https://doi.org/10.1029/2000JD900040, 2000.

Dufresne, J.-L., Gautier, C., Ricchiazzi, P., and Fouquart, Y.: Longwave Scattering Effects of Mineral Aerosols, Journal of the Atmospheric Sciences, 59, 1959–1966, https://doi.org/10.1175/1520-
850   0469(2002)059<1959:LSEOMA>2.0.CO;2, 2002.

Efron, B.: The jackknife, the bootstrap, and other resampling plans, Philadelphia, Pa.: Society for Industrial and Applied Mathematics (SIAM, 3600 Market Street, Floor 6, Philadelphia, PA 19104), 1 online resource (vii, 92 p.) pp., 1982.

Emmons, L. K., Schwantes, R. H., Orlando, J. J., Tyndall, G., Kinnison, D., Lamarque, J.-F., Marsh, D.,
855   Mills, M. J., Tilmes, S., Bardeen, C., Buchholz, R. R., Conley, A., Gettelman, A., Garcia, R., Simpson, I., Blake, D. R., Meinardi, S., and Pétron, G.: The Chemistry Mechanism in the Community Earth System Model Version 2 (CESM2), Journal of Advances in Modeling Earth Systems, 12, e2019MS001882, https://doi.org/10.1029/2019MS001882, 2020.

Evan, A. T.: Surface Winds and Dust Biases in Climate Models, Geophysical Research Letters, 45,
860   1079–1085, https://doi.org/10.1002/2017GL076353, 2018.

Ferrenberg, S., Reed, S. C., and Belnap, J.: Climate change and physical disturbance cause similar community shifts in biological soil crusts, Proceedings of the National Academy of Sciences, 112, 12116–12121, https://doi.org/10.1073/pnas.1509150112, 2015.

865 Ghan, S. J. and Zaveri, R. A.: Parameterization of optical properties for hydrated internally mixed aerosol, Journal of Geophysical Research: Atmospheres, 112, https://doi.org/10.1029/2006JD007927, 2007.

Ginoux, P., Prospero, J. M., Gill, T. E., Hsu, N. C., and Zhao, M.: Global-scale attribution of anthropogenic and natural dust sources and their emission rates based on MODIS Deep Blue aerosol products, Reviews of Geophysics, 50, https://doi.org/10.1029/2012RG000388, 2012.

870 Green, R. O., Mahowald, N., Ung, C., Thompson, D. R., Bator, L., Bennet, M., Bernas, M., Blackway, N., Bradley, C., Cha, J., Clark, P., Clark, R., Cloud, D., Diaz, E., Ben Dor, E., Duren, R., Eastwood, M., Ehlmann, B. L., Fuentes, L., Ginoux, P., Gross, J., He, Y., Kalashnikova, O., Kert, W., Keymeulen, D., Klimesh, M., Ku, D., Kwong-Fu, H., Liggett, E., Li, L., Lundeen, S., Makowski, M. D., Mazer, A., Miller, R., Mouroulis, P., Oaida, B., Okin, G. S., Ortega, A., Oyake, A., Nguyen, H., Pace, T., Painter, 875 T. H., Pempejian, J., Garcia-Pando, C. P., Pham, T., Phillips, B., Pollock, R., Purcell, R., Realmuto, V., Schoolcraft, J., Sen, A., Shin, S., Shaw, L., Soriano, M., Swayze, G., Thingvold, E., Vaid, A., and Zan, J.: The Earth Surface Mineral Dust Source Investigation: An Earth Science Imaging Spectroscopy Mission, in: 2020 IEEE Aerospace Conference, 2020 IEEE Aerospace Conference, Big Sky, MT, USA, 1–15, https://doi.org/10.1109/AERO47225.2020.9172731, 2020.

880 Groot Zwaaftink, C. D., Grythe, H., Skov, H., and Stohl, A.: Substantial contribution of northern high-latitude sources to mineral dust in the Arctic, Journal of Geophysical Research: Atmospheres, 121, 13,678-13,697, https://doi.org/10.1002/2016JD025482, 2016.

Hamilton, D. S., Perron, M. M. G., Bond, T. C., Bowie, A. R., Buchholz, R. R., Guieu, C., Ito, A., Maenhaut, W., Myriokefalitakis, S., Olgun, N., Rathod, S. D., Schepanski, K., Tagliabue, A., Wagner, 885 R., and Mahowald, N. M.: Earth, Wind, Fire, and Pollution: Aerosol Nutrient Sources and Impacts on Ocean Biogeochemistry, Annual Review of Marine Science, 14, 303–330, https://doi.org/10.1146/annurev-marine-031921-013612, 2022.

Held, I. M. and Soden, B. J.: Robust Responses of the Hydrological Cycle to Global Warming, Journal of Climate, 19, 5686–5699, https://doi.org/10.1175/JCLI3990.1, 2006.

890 Hess, M., Koepke, P., and Schult, I.: Optical Properties of Aerosols and Clouds: The Software Package OPAC, Bulletin of the American Meteorological Society, 79, 831–844, https://doi.org/10.1175/1520-0477(1998)079<0831:OPOAAC>2.0.CO;2, 1998.

Hooper, J. and Marx, S.: A global doubling of dust emissions during the Anthropocene?, Global and Planetary Change, 169, 70–91, https://doi.org/10.1016/j.gloplacha.2018.07.003, 2018.

895 Hurtt, G. C., Chini, L., Sahajpal, R., Frolking, S., Bodirsky, B. L., Calvin, K., Doelman, J. C., Fisk, J., Fujimori, S., Klein Goldewijk, K., Hasegawa, T., Havlik, P., Heinimann, A., Humpenöder, F., Jungclaus, J., Kaplan, J. O., Kennedy, J., Krisztin, T., Lawrence, D., Lawrence, P., Ma, L., Mertz, O., Pongratz, J., Popp, A., Poulter, B., Riahi, K., Shevliakova, E., Stehfest, E., Thornton, P., Tubiello, F. N., van Vuuren, D. P., and Zhang, X.: Harmonization of global land use change and management for the 900 period 850–2100 (LUH2) for CMIP6, Geoscientific Model Development, 13, 5425–5464, https://doi.org/10.5194/gmd-13-5425-2020, 2020.

Iacono, M. J., Delamere, J. S., Mlawer, E. J., Shephard, M. W., Clough, S. A., and Collins, W. D.: Radiative forcing by long-lived greenhouse gases: Calculations with the AER radiative transfer models, Journal of Geophysical Research: Atmospheres, 113, https://doi.org/10.1029/2008JD009944, 2008.

905  Indoitu, R., Kozhoridze, G., Batyrbaeva, M., Vitkovskaya, I., Orlovsky, N., Blumberg, D., and Orlovsky, L.: Dust emission and environmental changes in the dried bottom of the Aral Sea, Aeolian Research, 17, 101–115, https://doi.org/10.1016/j.aeolia.2015.02.004, 2015.

Ito, A., Adebiyi, A. A., Huang, Y., and Kok, J. F.: Less atmospheric radiative heating by dust due to the synergy of coarser size and aspherical shape, Atmospheric Chemistry and Physics, 21, 16869–16891, 910  https://doi.org/10.5194/acp-21-16869-2021, 2021.

Journet, E., Balkanski, Y., and Harrison, S. P.: A new data set of soil mineralogy for dust-cycle modeling, Atmos. Chem. Phys., 14, 3801–3816, https://doi.org/10.5194/acp-14-3801-2014, 2014.

Ke, Z., Liu, X., Wu, M., Shan, Y., and Shi, Y.: Improved Dust Representation and Impacts on Dust Transport and Radiative Effect in CAM5, Journal of Advances in Modeling Earth Systems, 14, 915  e2021MS002845, https://doi.org/10.1029/2021MS002845, 2022.

Klein Goldewijk, K., Beusen, A., van Drecht, G., and de Vos, M.: The HYDE 3.1 spatially explicit database of human-induced global land-use change over the past 12,000 years, Global Ecology and Biogeography, 20, 73–86, https://doi.org/10.1111/j.1466-8238.2010.00587.x, 2011.

Klose, M., Jorba, O., Gonçalves Ageitos, M., Escribano, J., Dawson, M. L., Obiso, V., Di Tomaso, E., 920  Basart, S., Montané Pinto, G., Macchia, F., Ginoux, P., Guerschman, J., Prigent, C., Huang, Y., Kok, J. F., Miller, R. L., and Pérez García-Pando, C.: Mineral dust cycle in the Multiscale Online Nonhydrostatic AtmospheRe CHemistry model (MONARCH) Version 2.0, Geosci. Model Dev., 14, 6403–6444, https://doi.org/10.5194/gmd-14-6403-2021, 2021.

Kok, J. F.: A scaling theory for the size distribution of emitted dust aerosols suggests climate models 925  underestimate the size of the global dust cycle, PNAS, 108, 1016–1021, https://doi.org/10.1073/pnas.1014798108, 2011.

Kok, J. F., Mahowald, N. M., Fratini, G., Gillies, J. A., Ishizuka, M., Leys, J. F., Mikami, M., Park, M.-S., Park, S.-U., Van Pelt, R. S., and Zobeck, T. M.: An improved dust emission model – Part 1: Model description and comparison against measurements, Atmospheric Chemistry and Physics, 14, 13023–930  13041, https://doi.org/10.5194/acp-14-13023-2014, 2014.

Kok, J. F., Ridley, D. A., Zhou, Q., Miller, R. L., Zhao, C., Heald, C. L., Ward, D. S., Albani, S., and Haustein, K.: Smaller desert dust cooling effect estimated from analysis of dust size and abundance, Nature Geosci, 10, 274–278, https://doi.org/10.1038/ngeo2912, 2017.

Kok, J. F., Ward, D. S., Mahowald, N. M., and Evan, A. T.: Global and regional importance of the direct 935  dust-climate feedback, Nature Communications, 9, 241, https://doi.org/10.1038/s41467-017-02620-y, 2018.

Kok, J. F., Adebiyi, A. A., Albani, S., Balkanski, Y., Checa-Garcia, R., Chin, M., Colarco, P. R., Hamilton, D. S., Huang, Y., Ito, A., Klose, M., Leung, D. M., Li, L., Mahowald, N. M., Miller, R. L., Obiso, V., Pérez García-Pando, C., Rocha-Lima, A., Wan, J. S., and Whicker, C. A.: Improved

940   representation of the global dust cycle using observational constraints on dust properties and abundance,
Atmos. Chem. Phys., 21, 8127–8167, https://doi.org/10.5194/acp-21-8127-2021, 2021a.

Kok, J. F., Adebiyi, A. A., Albani, S., Balkanski, Y., Checa-Garcia, R., Chin, M., Colarco, P. R.,
Hamilton, D. S., Huang, Y., Ito, A., Klose, M., Li, L., Mahowald, N. M., Miller, R. L., Obiso, V., Pérez
García-Pando, C., Rocha-Lima, A., and Wan, J. S.: Contribution of the world's main dust source regions
945   to the global cycle of desert dust, Atmos. Chem. Phys., 21, 8169–8193, https://doi.org/10.5194/acp-21-
8169-2021, 2021b.

Kok, J. F., Storelvmo, T., Karydis, V. A., Adebiyi, A. A., Mahowald, N. M., Evan, A. T., He, C., and
Leung, D. M.: Mineral dust aerosol impacts on global climate and climate change, Nat Rev Earth
Environ, 1–16, https://doi.org/10.1038/s43017-022-00379-5, 2023.

950   Lawrence, D. M., Fisher, R. A., Koven, C. D., Oleson, K. W., Swenson, S. C., Bonan, G., Collier, N.,
Ghimire, B., van Kampenhout, L., Kennedy, D., Kluzek, E., Lawrence, P. J., Li, F., Li, H.,
Lombardozzi, D., Riley, W. J., Sacks, W. J., Shi, M., Vertenstein, M., Wieder, W. R., Xu, C., Ali, A. A.,
Badger, A. M., Bisht, G., van den Broeke, M., Brunke, M. A., Burns, S. P., Buzan, J., Clark, M., Craig,
A., Dahlin, K., Drewniak, B., Fisher, J. B., Flanner, M., Fox, A. M., Gentine, P., Hoffman, F., Keppel-
955   Aleks, G., Knox, R., Kumar, S., Lenaerts, J., Leung, L. R., Lipscomb, W. H., Lu, Y., Pandey, A.,
Pelletier, J. D., Perket, J., Randerson, J. T., Ricciuto, D. M., Sanderson, B. M., Slater, A., Subin, Z. M.,
Tang, J., Thomas, R. Q., Val Martin, M., and Zeng, X.: The Community Land Model Version 5:
Description of New Features, Benchmarking, and Impact of Forcing Uncertainty, Journal of Advances
in Modeling Earth Systems, 11, 4245–4287, https://doi.org/10.1029/2018MS001583, 2019.

960   Leung, D. M., Kok, J. F., Li, L., Okin, G. S., Prigent, C., Klose, M., Pérez García-Pando, C., Menut, L.,
Mahowald, N. M., Lawrence, D. M., and Chamecki, M.: A new process-based and scale-aware desert
dust emission scheme for global climate models – Part I: Description and evaluation against inverse
modeling emissions, Atmospheric Chemistry and Physics, 23, 6487–6523, https://doi.org/10.5194/acp-
23-6487-2023, 2023.

965   Leung, D. M., Kok, J. F., Li, L., Mahowald, N. M., Lawrence, D. M., Tilmes, S., Kluzek, E., Klose, M.,
and Pérez García-Pando, C.: A new process-based and scale-aware desert dust emission scheme for
global climate models – Part II: Evaluation in the Community Earth System Model version 2 (CESM2),
Atmospheric Chemistry and Physics, 24, 2287–2318, https://doi.org/10.5194/acp-24-2287-2024, 2024.

Li, L. and Sokolik, I. N.: The Dust Direct Radiative Impact and Its Sensitivity to the Land Surface State
970   and Key Minerals in the WRF-Chem-DuMo Model: A Case Study of Dust Storms in Central Asia,
Journal of Geophysical Research: Atmospheres, 123, 4564–4582,
https://doi.org/10.1029/2017JD027667, 2018.

Li, L., Mahowald, N. M., Miller, R. L., Pérez García-Pando, C., Klose, M., Hamilton, D. S., Gonçalves
Ageitos, M., Ginoux, P., Balkanski, Y., Green, R. O., Kalashnikova, O., Kok, J. F., Obiso, V., Paynter,
975   D., and Thompson, D. R.: Quantifying the range of the dust direct radiative effect due to source
mineralogy uncertainty, Atmospheric Chemistry and Physics, 21, 3973–4005,
https://doi.org/10.5194/acp-21-3973-2021, 2021a.

Li, L., Mahowald, N. M., Kok, J. F., Liu, X., Wu, M., Leung, D. M., Hamilton, D. S., Emmons, L. K.,
Huang, Y., Sexton, N., Meng, J., and Wan, J.: Importance of different parameterization changes for the
980   updated dust cycle modeling in the Community Atmosphere Model (version 6.1), Geosci. Model Dev.,
15, 8181–8219, https://doi.org/10.5194/gmd-15-8181-2022, 2022.

Li, Y., Mickley, L. J., and Kaplan, J. O.: Response of dust emissions in southwestern North America to 21st century trends in climate, $CO_2$ fertilization, and land use: implications for air quality, Atmospheric Chemistry and Physics, 21, 57–68, https://doi.org/10.5194/acp-21-57-2021, 2021b.

985   Liu, J., Wang, X., Wu, D., Wei, H., Li, Y., and Ji, M.: Historical footprints and future projections of global dust burden from bias-corrected CMIP6 models, npj Clim Atmos Sci, 7, 1–12, https://doi.org/10.1038/s41612-023-00550-9, 2024.

Liu, X., Ma, P.-L., Wang, H., Tilmes, S., Singh, B., Easter, R. C., Ghan, S. J., and Rasch, P. J.: Description and evaluation of a new four-mode version of the Modal Aerosol Module (MAM4) within
990   version 5.3 of the Community Atmosphere Model, Geosci. Model Dev., 9, 505–522, https://doi.org/10.5194/gmd-9-505-2016, 2016.

Logothetis, S.-A., Salamalikis, V., Gkikas, A., Kazadzis, S., Amiridis, V., and Kazantzidis, A.: 15-year variability of desert dust optical depth on global and regional scales, Atmospheric Chemistry and Physics, 21, 16499–16529, https://doi.org/10.5194/acp-21-16499-2021, 2021.

995   Mahowald, N. M.: Anthropocene changes in desert area: Sensitivity to climate model predictions, Geophysical Research Letters, 34, https://doi.org/10.1029/2007GL030472, 2007.

Mahowald, N. M. and Luo, C.: A less dusty future?, Geophysical Research Letters, 30, https://doi.org/10.1029/2003GL017880, 2003.

Mahowald, N. M., Kloster, S., Engelstaedter, S., Moore, J. K., Mukhopadhyay, S., McConnell, J. R.,
1000   Albani, S., Doney, S. C., Bhattacharya, A., Curran, M. A. J., Flanner, M. G., Hoffman, F. M., Lawrence, D. M., Lindsay, K., Mayewski, P. A., Neff, J., Rothenberg, D., Thomas, E., Thornton, P. E., and Zender, C. S.: Observed 20th century desert dust variability: impact on climate and biogeochemistry, Atmos. Chem. Phys., 10, 10875–10893, https://doi.org/10.5194/acp-10-10875-2010, 2010.

Mahowald, N. M., Li, L., Albani, S., Hamilton, D. S., and Kok, J. F.: Opinion: The importance of
1005   historical and paleoclimate aerosol radiative effects, Atmospheric Chemistry and Physics, 24, 533–551, https://doi.org/10.5194/acp-24-533-2024, 2024.

Masson-Delmotte, V., Zhai, P., Pirani, A., Connors, S. L., Péan, C., Berger, S., Caud, N., Chen, Y., Goldfarb, L., and Gomis, M.: Climate change 2021: the physical science basis, Contribution of working group I to the sixth assessment report of the intergovernmental panel on climate change, 2, 2391, 2021.

1010   McConnell, J. R., Aristarain, A. J., Banta, J. R., Edwards, P. R., and Simões, J. C.: 20th-Century doubling in dust archived in an Antarctic Peninsula ice core parallels climate change and desertification in South America, Proceedings of the National Academy of Sciences, 104, 5743–5748, https://doi.org/10.1073/pnas.0607657104, 2007.

Mulitza, S., Heslop, D., Pittauerova, D., Fischer, H. W., Meyer, I., Stuut, J.-B., Zabel, M., Mollenhauer,
1015   G., Collins, J. A., Kuhnert, H., and Schulz, M.: Increase in African dust flux at the onset of commercial agriculture in the Sahel region, Nature, 466, 226–228, https://doi.org/10.1038/nature09213, 2010.

Neale, R. B., Gettelman, A., Park, S., Chen, C.-C., Lauritzen, P. H., Williamson, D. L., Conley, A. J., Kinnison, D., Marsh, D., Smith, A. K., Vitt, F., Garcia, R., Lamarque, J.-F., Mills, M., Tilmes, S., Morrison, H., Cameron-Smith, P., Collins, W. D., Iacono, M. J., Easter, R. C., Liu, X., Ghan, S. J.,

1020   Rasch, P. J., and Taylor, M. A.: Description of the NCAR Community Atmosphere Model (CAM 5.0), 289, 2012.

Neff, J. C., Ballantyne, A. P., Farmer, G. L., Mahowald, N. M., Conroy, J. L., Landry, C. C., Overpeck, J. T., Painter, T. H., Lawrence, C. R., and Reynolds, R. L.: Increasing eolian dust deposition in the western United States linked to human activity, Nature Geosci, 1, 189–195,
1025   https://doi.org/10.1038/ngeo133, 2008.

Niemeyer, T. C., Gillette, D. A., DeLuisi, J. J., Kim, Y. J., Niemeyer, W. F., Ley, T., Gill, T. E., and Ono, D.: Optical depth, size distribution and flux of dust from Owens Lake, California, Earth Surface Processes and Landforms, 24, 463–479, https://doi.org/10.1002/(SICI)1096-9837(199905)24:5<463::AID-ESP2>3.0.CO;2-R, 1999.

1030   Pincus, R., Mlawer, E. J., and Delamere, J. S.: Balancing Accuracy, Efficiency, and Flexibility in Radiation Calculations for Dynamical Models, Journal of Advances in Modeling Earth Systems, 11, 3074–3089, https://doi.org/10.1029/2019MS001621, 2019.

Prospero, J. M., Delany, A. C., Delany, A. C., and Carlson, T. N.: The Discovery of African Dust Transport to the Western Hemisphere and the Saharan Air Layer: A History, Bulletin of the American
1035   Meteorological Society, 102, E1239–E1260, https://doi.org/10.1175/BAMS-D-19-0309.1, 2021.

Pu, B. and Ginoux, P.: Projection of American dustiness in the late 21st century due to climate change, Sci Rep, 7, 5553, https://doi.org/10.1038/s41598-017-05431-9, 2017.

Rayner, N. A., Parker, D. E., Horton, E. B., Folland, C. K., Alexander, L. V., Rowell, D. P., Kent, E. C., and Kaplan, A.: Global analyses of sea surface temperature, sea ice, and night marine air temperature
1040   since the late nineteenth century, Journal of Geophysical Research: Atmospheres, 108, https://doi.org/10.1029/2002JD002670, 2003.

Ridley, D. A., Heald, C. L., Kok, J. F., and Zhao, C.: An observationally constrained estimate of global dust aerosol optical depth, Atmospheric Chemistry and Physics, 16, 15097–15117, https://doi.org/10.5194/acp-16-15097-2016, 2016.

1045   Rodriguez-Caballero, E., Belnap, J., Büdel, B., Crutzen, P. J., Andreae, M. O., Pöschl, U., and Weber, B.: Dryland photoautotrophic soil surface communities endangered by global change, Nature Geosci, 11, 185–189, https://doi.org/10.1038/s41561-018-0072-1, 2018.

Rodriguez-Caballero, E., Stanelle, T., Egerer, S., Cheng, Y., Su, H., Canton, Y., Belnap, J., Andreae, M. O., Tegen, I., Reick, C. H., Pöschl, U., and Weber, B.: Global cycling and climate effects of aeolian dust
1050   controlled by biological soil crusts, Nat. Geosci., 15, 458–463, https://doi.org/10.1038/s41561-022-00942-1, 2022.

Schutgens, N., Tsyro, S., Gryspeerdt, E., Goto, D., Weigum, N., Schulz, M., and Stier, P.: On the spatio-temporal representativeness of observations, Atmospheric Chemistry and Physics, 17, 9761–9780, https://doi.org/10.5194/acp-17-9761-2017, 2017.

1055   Skiles, S. M., Flanner, M., Cook, J. M., Dumont, M., and Painter, T. H.: Radiative forcing by light-absorbing particles in snow, Nature Clim Change, 8, 964–971, https://doi.org/10.1038/s41558-018-0296-5, 2018.

Smith, M. B., Mahowald, N. M., Albani, S., Perry, A., Losno, R., Qu, Z., Marticorena, B., Ridley, D. A., and Heald, C. L.: Sensitivity of the interannual variability of mineral aerosol simulations to meteorological forcing dataset, Atmos. Chem. Phys., 17, 3253–3278, https://doi.org/10.5194/acp-17-3253-2017, 2017.

Smith, S. D., Huxman, T. E., Zitzer, S. F., Charlet, T. N., Housman, D. C., Coleman, J. S., Fenstermaker, L. K., Seemann, J. R., and Nowak, R. S.: Elevated CO2 increases productivity and invasive species success in an arid ecosystem, Nature, 408, 79–82, https://doi.org/10.1038/35040544, 2000.

Sokolik, I. N. and Toon, O. B.: Direct radiative forcing by anthropogenic airborne mineral aerosols, Nature, 381, 681–683, https://doi.org/10.1038/381681a0, 1996.

Stanelle, T., Bey, I., Raddatz, T., Reick, C., and Tegen, I.: Anthropogenically induced changes in twentieth century mineral dust burden and the associated impact on radiative forcing, Journal of Geophysical Research: Atmospheres, 119, 13,526-13,546, https://doi.org/10.1002/2014JD022062, 2014.

Storelvmo, T.: Aerosol Effects on Climate via Mixed-Phase and Ice Clouds, Annual Review of Earth and Planetary Sciences, 45, 199–222, https://doi.org/10.1146/annurev-earth-060115-012240, 2017.

Tegen, I. and Lacis, A. A.: Modeling of particle size distribution and its influence on the radiative properties of mineral dust aerosol, Journal of Geophysical Research: Atmospheres, 101, 19237–19244, https://doi.org/10.1029/95JD03610, 1996.

Tegen, I., Werner, M., Harrison, S. P., and Kohfeld, K. E.: Relative importance of climate and land use in determining present and future global soil dust emission, Geophysical Research Letters, 31, https://doi.org/10.1029/2003GL019216, 2004.

Thornhill, G., Collins, W., Olivié, D., Skeie, R. B., Archibald, A., Bauer, S., Checa-Garcia, R., Fiedler, S., Folberth, G., Gjermundsen, A., Horowitz, L., Lamarque, J.-F., Michou, M., Mulcahy, J., Nabat, P., Naik, V., O'Connor, F. M., Paulot, F., Schulz, M., Scott, C. E., Séférian, R., Smith, C., Takemura, T., Tilmes, S., Tsigaridis, K., and Weber, J.: Climate-driven chemistry and aerosol feedbacks in CMIP6 Earth system models, Atmospheric Chemistry and Physics, 21, 1105–1126, https://doi.org/10.5194/acp-21-1105-2021, 2021.

Wagner, R., Schepanski, K., and Klose, M.: The Dust Emission Potential of Agricultural-Like Fires—Theoretical Estimates From Two Conceptually Different Dust Emission Parameterizations, Journal of Geophysical Research: Atmospheres, 126, e2020JD034355, https://doi.org/10.1029/2020JD034355, 2021.

Wang, S. S.-C., Leung, L. R., and Qian, Y.: Projection of Future Fire Emissions Over the Contiguous US Using Explainable Artificial Intelligence and CMIP6 Models, Journal of Geophysical Research: Atmospheres, 128, e2023JD039154, https://doi.org/10.1029/2023JD039154, 2023.

Webb, N. P. and Pierre, C.: Quantifying Anthropogenic Dust Emissions, Earth's Future, 6, 286–295, https://doi.org/10.1002/2017EF000766, 2018.

Wilks, D. S.: Statistical Methods in the Atmospheric Sciences, Academic Press, 698 pp., 2011.

1095    Wu, C., Lin, Z., Shao, Y., Liu, X., and Li, Y.: Drivers of recent decline in dust activity over East Asia, Nat Commun, 13, 7105, https://doi.org/10.1038/s41467-022-34823-3, 2022.

Xi, X. and Sokolik, I. N.: Quantifying the anthropogenic dust emission from agricultural land use and desiccation of the Aral Sea in Central Asia, Journal of Geophysical Research: Atmospheres, 121, 12,270-12,281, https://doi.org/10.1002/2016JD025556, 2016.

1100    Yu, Y. and Ginoux, P.: Enhanced dust emission following large wildfires due to vegetation disturbance, Nat. Geosci., 15, 878–884, https://doi.org/10.1038/s41561-022-01046-6, 2022.

Zender, C. S., Bian, H., and Newman, D.: Mineral Dust Entrainment and Deposition (DEAD) model: Description and 1990s dust climatology, Journal of Geophysical Research: Atmospheres, 108, https://doi.org/10.1029/2002JD002775, 2003.

1105    Zhang, L., Gong, S., Padro, J., and Barrie, L.: A size-segregated particle dry deposition scheme for an atmospheric aerosol module, Atmospheric Environment, 35, 549–560, https://doi.org/10.1016/S1352-2310(00)00326-5, 2001.

Zhao, A., Ryder, C. L., and Wilcox, L. J.: How well do the CMIP6 models simulate dust aerosols?, Atmospheric Chemistry and Physics, 22, 2095–2119, https://doi.org/10.5194/acp-22-2095-2022, 2022.

1110    Zuidema, P., Alvarez, C., Kramer, S. J., Custals, L., Izaguirre, M., Sealy, P., Prospero, J. M., and Blades, E.: Is Summer African Dust Arriving Earlier to Barbados? The Updated Long-Term In Situ Dust Mass Concentration Time Series from Ragged Point, Barbados, and Miami, Florida, Bulletin of the American Meteorological Society, 100, 1981–1986, https://doi.org/10.1175/BAMS-D-18-0083.1, 2019.